Journal of Sound and Vibration (2002) **250**(4), 675–709
doi:10.1006/jsvi.2001.3949, available online at http://www.idealibrary.com on IDEAL®

VIBRATION OF A COMPLIANT TOWER IN THREE-DIMENSIONS

S. M. Han† and H. Benaroya

Department of Mechanical and Aerospace Engineering, Rutgers, the State University of New Jersey, Piscataway, 98 Brett Road, NJ 08854-8058, *U.S.A.*

(*Received* 2 *February* 2001, *and in final form* 10 *August* 2001)

The three-dimensional motion of an offshore compliant tower using both rigid and flexible beam models is studied in this paper. The tower is modelled as a beam supported by a torsional spring at the base with a point mass at the free end. The torsional spring constant is the same in all directions. When the beam is considered rigid, the two-degree-of-freedom model is employed. The two degrees constitute the two angular degrees of spherical co-ordinates, and the resulting equations are coupled and non-linear. When the beam is considered as elastic, three displacements are obtained as functions of the axial co-ordinate and time; again with coupled and non-linear equations of motion. The free and the forced responses due to deterministic loads are presented. The free responses of the rigid and elastic beams show rotating elliptical paths when viewed from above. The rate at which the path rotates depends on the initial conditions. When a harmonic transverse loading is applied in one direction, the displacement in that direction shows subharmonic resonance of order 1/2 and 1/3 while the displacement in the perpendicular direction is affected minimally. Next, in addition to the harmonic load in one direction, a transverse load is applied in the perpendicular direction. The transverse load varies exponentially with depth but is constant with time. It is found that the transverse load affects the transverse displacements in the perpendicular direction minimally.

1. INTRODUCTION

The purpose of this paper is to show how to model and predict three-dimensional responses of a structure in an ocean environment. Offshore structures are used in the oil industry as exploratory, production, oil storage, and oil landing facilities. Detailed specifications and descriptions can be found in *Hydrodynamic of Offshore Structures* by Chakrabarti [1].

Offshore structures are designed to be self-supporting and sufficiently stable for offshore operations such as drilling and production of oil. In general, there are two types of stationary offshore structures: fixed and compliant. Fixed structures are designed to withstand environmental forces without any substantial displacement. Compliant structures, on the other hand, are designed to allow small but not negligible deformation and deflection. While the stability of fixed structures is provided by structural rigidity, the stability of compliant structures is provided by tension due to buoyancy chambers. For these compliant structures, the dynamic responses need to be explored fully.

The fixed structures are economically feasible only up to water depths in the range of 300–500 m. Fixed platforms are indeed the most popular and prolific structures for water depths of 100–200 m. However, they become impractical for deep water because they must

†Currently at the Woods Hole Oceanographic Institution.

0022-460X/02/090675 + 35 $35.00/0

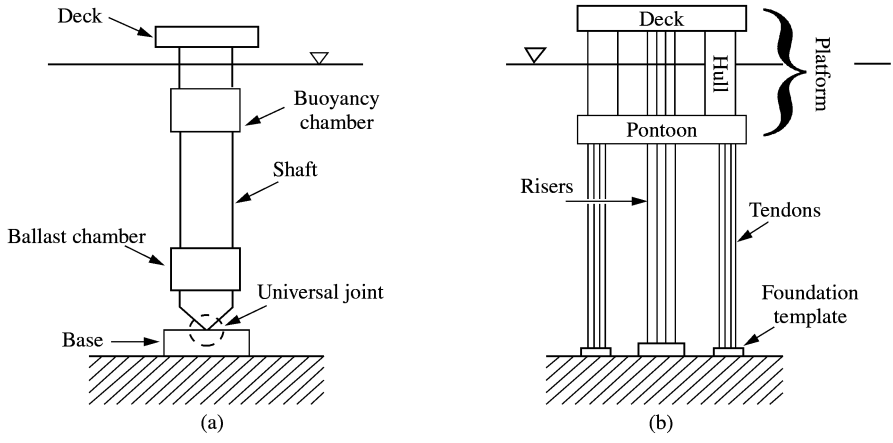

Figure 1. Offshore compliant towers: (a) articulated tower; (b) tension leg platform (TLP).

be built stronger and bulkier than the equivalent compliant structures. In recent years, the need to explore deeper water has made compliant structures more popular. Compliant towers are believed to be economically feasible in water depths exceeding 600 m.

Here, we will consider compliant structures. In particular, we are interested in articulated towers and tension leg platforms (TLP) as shown in Figure 1. An articulated tower includes a ballast chamber near the bottom, a buoyancy chamber near the surface of the water, and a shaft in between. A TLP is vertically moored by tendons at each corner of the platform. Buoyancy is provided by the fully submerged pontoon and partially submerged hulls. Risers are production-related pipes.

An offshore structure in an ocean environment is subjected to loadings due to wind, current, and waves. When the fluid passes by the structure, it exerts forces in the direction of the flow due to inertia, drag, and added mass effects. The inertia force is the force exerted by the fluid as it accelerates and decelerates around the structure. The drag force is due to the pressure difference between the downstream and upstream region. The added mass effect is due to the fact that the surrounding fluid is accelerated with the structure.

As well as these *in-plane* fluid forces, the fluid also exerts a lift force in the direction *perpendicular* to the flow and the structure. When the flow passes around a cylinder at a Reynolds number greater than 40, the vortices attached to the cylinder start to shed alternately creating the well-known von Kármán vortex street. These vortices exert an oscillatory force on the cylinder in the direction perpendicular to both the flow and the structure.

Therefore, the vibration of an offshore structure in an ocean environment is inherently a three-dimensional phenomenon. When the dynamic response of a compliant tower in an ocean environment is considered, the vertical member of the tower is modelled as either rigid or elastic. The three-dimensional behavior of the rigid model has been studied by Jain and Kirk [2] and Bar-Avi and Benaroya [3]. The former used two rigid beams in order to model a double-articulated offshore structure, and the latter used one rigid beam for a single articulated offshore structure. In their derivations, the spherical co-ordinates are used to describe the motion of the beam. Jain and Kirk showed that if the waves and the current are collinear, the response is two dimensional, but if the fluid motions are not collinear, the response is three-dimensional whirling oscillation.

So far, most elastic models are planar models so that only forces in one plane can be included. Adrezin and Benaroya [4, 5] examined the non-linear transverse behavior of

a tension leg platform with time-dependent tension due to gravity and buoyancy, which depended on the current configuration of the structure. Han and Benaroya [6, 7] investigated the non-linear coupled transverse and axial responses. They both used finite difference methods. McNamara and Lane [8] and Sebastiani *et al.* [9] used finite element models. In all cases, only the response due to in-plane fluid force was examined.

Leonard and Young [10] developed a three-dimensional finite element method. They saw behaviors similar to those observed in reference [2] in their study of rigid models.

A compliant tower is designed to be flexible. Therefore, the rigid model may not be sufficient. On the other hand, flexible models with fluid forces confined to one plane do not capture the three-dimensional aspects of the problem. Therefore, in this paper, we devise a flexible model that can include the fluid forces in three dimensions. The equations of motion are solved numerically using the finite difference method.

First, the equations of motion of the three-dimensional model are derived for two cases: rigid structure and elastic structure. Second, the free responses of the rigid and the elastic models are compared. The free response obtained using the rigid model allows us to gain confidence in the formulation and the numerical results obtained using the elastic model. Finally, the forced responses due to deterministic loads are investigated. Two cases are studied in particular. The first case is when a harmonic (in time) load is applied in one direction, and the second case is when steady and harmonic loads are applied in mutually perpendicular directions. The second case can be thought of as the three-dimensional loading arising from a current that also induces vortex shedding. The responses due to these simple fluid force models will prepare us for the study of responses due to more complicated fluid loading models.

2. MATHEMATICAL FORMULATIONS

2.1. RIGID MODEL

In this study, the vertical member of an articulated tower or a leg of a tension leg platform is modelled as a smooth cylindrical beam, the support at the base as a torsional spring, and the structures above the water line as a point mass. It is assumed that the base of the torsional spring is free to rotate in any direction.

The equations of motion when the beam is considered rigid are derived in this section. From Figure 2, the system can be described with two angular degrees of freedom. The equations of motion for a similar system were obtained in references [2, 3]. The equations of motion are re-derived here.

The kinetic energy of the system is given by

$$KE = \tfrac{1}{2}\{\omega\}^{\mathrm{T}}[I_0]\ \{\omega\} + \tfrac{1}{2} M_p \{V_p\}^{\mathrm{T}}\{V_p\}, \tag{1}$$

where $[I_0]$ is the mass moment of inertia matrix of the beam about the base, M_p is the point mass, and V_p is the velocity of the point mass. The first term is the kinetic energy of the beam, and the second term is the kinetic energy of the point mass.

We consider three frames of reference, xyz, $x'y'z'$, and $x_by_bz_b$, as shown in Figure 3. xyz is the inertial reference frame, $x'y'z'$ is obtained by rotating xyz by angle ϕ about the x-axis. $x_by_bz_b$ is obtained by rotating $x'y'z'$ by θ about the z'-axis. $x_by_bz_b$ is also called the body frame of reference since x_b-axis coincides with the axis of the beam.

The beam experiences two angular velocities, $\dot{\phi}$ about the x-axis and $\dot{\theta}$ about the z'-axis. The angular velocity of the beam is then

$$\boldsymbol{\omega} = \dot{\phi}\mathbf{i} + \dot{\theta}\mathbf{k}', \tag{2}$$

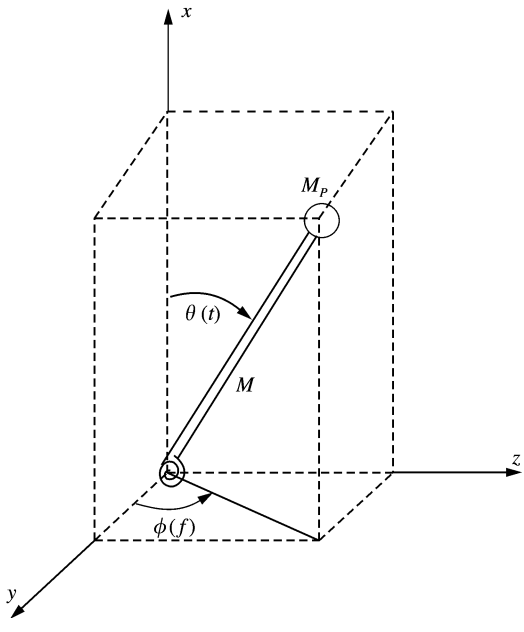

Figure 2. Rigid beam model.

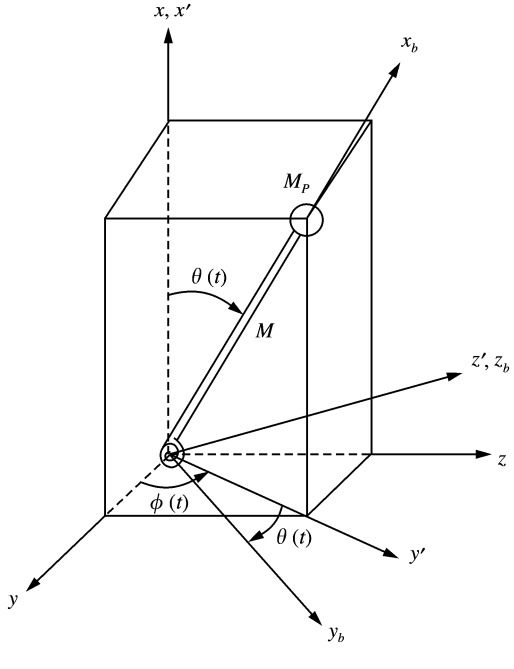

Figure 3. Reference and body frames.

where $\mathbf{i}$ and $\mathbf{k}'$ are unit vectors in the x and z' directions respectively. We choose to express the angular velocity in the body frame of reference. The transformations between the unit vectors $\mathbf{i}$ and $\mathbf{k}'$ and the unit vectors of the body frame of reference are

$$\mathbf{i} = \cos\theta\mathbf{i}_b - \sin\theta\mathbf{j}_b, \qquad \mathbf{k}' = \mathbf{k}_b. \tag{3}$$

Therefore, the angular velocity in the body frame of reference is given by

$$\boldsymbol{\omega} = \dot{\phi}\cos\theta\mathbf{i}_b - \dot{\phi}\sin\theta\mathbf{j}_b + \dot{\theta}\mathbf{k}_b, \tag{4}$$

or in matrix form,

$$\{\omega\} = \begin{bmatrix} \dot{\phi}\cos\theta \\ -\dot{\phi}\sin\theta \\ \dot{\theta} \end{bmatrix}_{x_b y_b z_b}. \tag{5}$$

The mass moment of inertia about the base expressed in the body frame of reference is given by

$$[I_0] = \begin{bmatrix} \frac{1}{2}M(r_o^2 + r_i^2) & 0 & 0 \\ 0 & \frac{1}{4}M(r_o^2 + r_i^2) + \frac{1}{3}ML^2 & 0 \\ 0 & 0 & \frac{1}{4}M(r_o^2 + r_i^2) + \frac{1}{3}ML^2 \end{bmatrix}_{x_b y_b z_b}, \tag{6}$$

where r_o and r_i are the outer and inner radius of the beam, M is the total mass of the beam, and L is the length of the beam.

The kinetic energy of the beam is given by

$$\begin{aligned} KE_{beam} &= \tfrac{1}{2}\{\omega\}^{\mathrm{T}}[I_0]\{\omega\} \\ &= \tfrac{1}{4}M(r_o^2 + r_i^2)\dot{\phi}^2\cos^2\theta + \tfrac{1}{2}(\tfrac{1}{4}M(r_o^2 + r_i^2) + \tfrac{1}{3}ML^2)\dot{\phi}^2\sin^2\theta \\ &\quad + \dot{\theta}^2(\tfrac{1}{4}M(r_o^2 + r_i^2) + \tfrac{1}{3}ML^2). \end{aligned} \tag{7}$$

The velocity of the point mass is expressed in the inertial frame of reference. First, the displacement of the point mass is

$$\mathbf{r}_p = L\cos\theta\mathbf{i} + L\sin\theta\cos\phi\mathbf{j} + L\sin\theta\sin\phi\mathbf{k}. \tag{8}$$

The velocity is obtained by taking the derivative with respect to time. Since the displacement is expressed in the inertial frame, the derivatives of the unit vectors are zero. The velocity of the point mass is then given by

$$\{V_p\} = L\begin{bmatrix} -\dot{\theta}\sin\theta \\ \dot{\theta}\cos\theta\cos\phi - \dot{\phi}\sin\theta\sin\phi \\ \dot{\theta}\cos\theta\sin\phi + \dot{\phi}\sin\theta\cos\phi \end{bmatrix}_{xyz}. \tag{9}$$

The kinetic energy of the point mass is then

$$\begin{aligned} KE_{point\ mass} &= \tfrac{1}{2}M_p\{V_p\}^{\mathrm{T}}\{V_p\} \\ &= \tfrac{1}{2}M_pL^2(\dot{\theta}^2\sin^2\theta + \dot{\theta}\cos^2\theta\cos^2\phi - 2\dot{\theta}\dot{\phi}\cos\theta\cos\phi\sin\theta\sin\phi \\ &\quad + \dot{\phi}^2\sin^2\theta\sin^2\phi + \dot{\theta}^2\cos^2\theta\sin^2\phi + 2\dot{\theta}\dot{\phi}\cos\theta\sin\phi\sin\theta\cos\phi \\ &\quad + \dot{\phi}^2\sin^2\theta\cos^2\phi) \\ &= \tfrac{1}{2}M_pL^2(\dot{\theta}^2 + \dot{\phi}^2\sin^2\theta). \end{aligned} \tag{10}$$

Combining equations (7) and (10), the kinetic energy of the system is given by

$$KE = \tfrac{1}{2} J_2 (\dot{\theta}^2 + \dot{\phi}^2 \sin^2 \theta) + \tfrac{1}{2} J_1 \dot{\phi}^2 \cos^2 \theta, \tag{11}$$

where we let

$$J_1 = \tfrac{1}{2} M(r_o^2 + r_i^2), \quad J_2 = \tfrac{1}{3} ML^2 + M_p L^2 + \tfrac{1}{4} M(r_o^2 + r_i^2). \tag{12}$$

The potential energy is stored in the torsional spring and is given by

$$PE = \tfrac{1}{2} k\theta^2. \tag{13}$$

This assumes that the structure can only bend, not twist. Therefore, the Lagrangian is given by

$$\mathscr{L} = \tfrac{1}{2} [\tfrac{1}{3} ML^2 + M_p L^2 + \tfrac{1}{4} M(r_o^2 + r_i^2)] (\dot{\theta}^2 + \dot{\phi}^2 \sin^2 \theta) + \tfrac{1}{4} M(r_o^2 + r_i^2) \dot{\phi}^2 \cos^2 \theta - \tfrac{1}{2} k\theta^2. \tag{14}$$

Lagrange's equations are given by

$$\frac{\mathrm{d}}{\mathrm{d}t} \left(\frac{\partial \mathscr{L}}{\partial \dot{q}_k} \right) - \frac{\partial \mathscr{L}}{\partial q_k} = Q_{knc}, \quad k = 1, 2, \tag{15}$$

where Q_{knc} is the generalized non-conservative force associated with q_k, and q_1 and q_2 are θ and ϕ respectively. For an unforced system, the equations of motion are given by

$$J_2 \ddot{\theta} - (J_2 - J_1) \dot{\phi}^2 \sin \theta \cos \theta + k\theta = 0, \tag{16}$$

$$\frac{\mathrm{d}}{\mathrm{d}t} [\dot{\phi} (J_2 \sin^2 \theta + J_1 \cos^2 \theta)] = 0, \tag{17}$$

where J_1 and J_2 are given in equation (12). Note that equation (17) implies that $\phi(t)$ is a cyclic or ignorable co-ordinate, and the generalized momentum associated with $\phi(t)$, $\dot{\phi}(J_2 \sin^2 \theta + J_1 \cos^2 \theta)$, is conserved as long as $Q_{\phi nc}$ is zero.

2.2. ELASTIC MODEL

When the vertical member is modelled as a flexible structure, certain assumptions are made in order to simplify the problem. In addition to the assumptions used in the planar Euler–Bernoulli beam model [6], it is assumed that the rotation of the beam element can be moderate but the strain is small.

In this section, the displacement field is obtained using Kirchhoff's hypothesis, and the corresponding strain and stress fields are obtained accordingly. The potential and kinetic energies are then obtained to form the Lagrangian. The equations of motion are obtained using Hamilton's principle.

2.2.1. *Displacements, strains, and stress*

Using Kirchhoff's hypothesis, the displacement field is given by

$$u_1 = u(X, t) - Y\frac{\partial u_2(X, t)}{\partial X} - Z\frac{\partial u_3(X, t)}{\partial X},$$

$$u_2 = v(X, t), \quad u_3 = w(X, t), \tag{18}$$

where u_1, u_2, and u_3 are displacements in the x, y, and z directions respectively. u, v, and w are the mid-plane displacements of the cross-section in the x, y, and z directions respectively. They are also the average displacements for a symmetric cross-section. It should be noted that the displacements are measured from the original configuration as shown in Figure 4. The co-ordinates X, Y, and Z mark the original location of a beam element. Note that the average displacements are functions of X and t only.

The form of the displacement field implies that the shear effect is negligible when compared to that of the bending moment. Therefore, we are assuming that the beam is slender enough so that such an assumption is valid. Also, even though it is not obvious from the displacement field, Novozhilov [12] showed that the strains need to be small when compared to the rotation in order for the Kirchhoff's hypothesis to be valid. In mathematical terms,

$$\frac{\partial u_1}{\partial X} \sim \left(\frac{\partial u_2}{\partial X}\right)^2 \sim \left(\frac{\partial u_3}{\partial X}\right)^2 \ll 1. \tag{19}$$

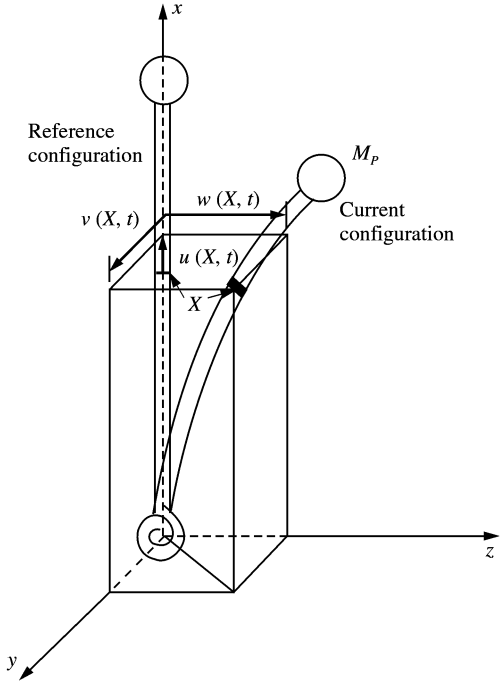

Figure 4. Three-dimensional beam model.

The general form of the Green strains are given by

$$\mathscr{E}_{11} = \frac{\partial u_1}{\partial X} + \frac{1}{2}\left[\left(\frac{\partial u_1}{\partial X}\right)^2 + \left(\frac{\partial u_2}{\partial X}\right)^2 + \left(\frac{\partial u_3}{\partial X}\right)^2\right],$$

$$\mathscr{E}_{22} = \frac{\partial u_2}{\partial Y} + \frac{1}{2}\left[\left(\frac{\partial u_1}{\partial Y}\right)^2 + \left(\frac{\partial u_2}{\partial Y}\right)^2 + \left(\frac{\partial u_3}{\partial Y}\right)^2\right],$$

$$\mathscr{E}_{33} = \frac{\partial u_3}{\partial Z} + \frac{1}{2}\left[\left(\frac{\partial u_1}{\partial Z}\right)^2 + \left(\frac{\partial u_2}{\partial Z}\right)^2 + \left(\frac{\partial u_3}{\partial Z}\right)^2\right],$$

$$\mathscr{E}_{12} = \frac{1}{2}\left[\frac{\partial u_2}{\partial X} + \frac{\partial u_1}{\partial Y} + \frac{\partial u_1}{\partial X}\frac{\partial u_1}{\partial Y} + \frac{\partial u_2}{\partial X}\frac{\partial u_2}{\partial Y} + \frac{\partial u_3}{\partial X}\frac{\partial u_3}{\partial Y}\right],$$

$$\mathscr{E}_{23} = \frac{1}{2}\left[\frac{\partial u_3}{\partial Y} + \frac{\partial u_2}{\partial Z} + \frac{\partial u_1}{\partial Y}\frac{\partial u_1}{\partial Z} + \frac{\partial u_2}{\partial Y}\frac{\partial u_2}{\partial Z} + \frac{\partial u_3}{\partial Y}\frac{\partial u_3}{\partial Z}\right],$$

$$\mathscr{E}_{13} = \frac{1}{2}\left[\frac{\partial u_3}{\partial X} + \frac{\partial u_1}{\partial Z} + \frac{\partial u_1}{\partial X}\frac{\partial u_1}{\partial Z} + \frac{\partial u_2}{\partial X}\frac{\partial u_2}{\partial Z} + \frac{\partial u_3}{\partial X}\frac{\partial u_3}{\partial Z}\right]. \tag{20}$$

Using equation (19) and substituting the displacement field in equation (18) into equation (20), the Green strains are then given by

$$\mathscr{E}_{11} = \frac{\partial u_1}{\partial X} + \frac{1}{2}\left[\left(\frac{\partial u_2}{\partial X}\right)^2 + \left(\frac{\partial u_3}{\partial X}\right)^2\right]$$

$$= u' - Yv'' + Zw'' + \tfrac{1}{2}v'^2 + \tfrac{1}{2}w'^2,$$

$$\mathscr{E}_{12} = \mathscr{E}_{22} = \mathscr{E}_{33} = \mathscr{E}_{23} = \mathscr{E}_{13} = 0. \tag{21}$$

The notations used are: $(') \equiv \partial/\partial X$ and $(\dot{}) \equiv \partial/\partial t$.

2.2.2. *Potential and kinetic energies*

The strain energy is given by

$$PE_{strain} = \frac{1}{2}\int_{V_0} \tilde{\sigma}_{ij}\mathscr{E}_{ij}\,\mathrm{d}V_0, \tag{22}$$

where $\tilde{\sigma}$ is the second Piola–Kirchhoff stress. Since $\mathscr{E}_{11}$ is the only non-zero strain, the strain energy is simply

$$PE_{strain} = \frac{1}{2}\int_0^L \int_{A_0} \tilde{\sigma}_{11}\mathscr{E}_{11}\,\mathrm{d}A_0\,\mathrm{d}X. \tag{23}$$

The stress is related to strain by the constitutive relationship given by

$$\tilde{\sigma}_{ij} = \lambda \mathscr{E}_{kk} \delta_{ij} + 2G\mathscr{E}_{ij}. \tag{24}$$

The stress, $\tilde{\sigma}_{11}$, is then

$$\begin{aligned} \tilde{\sigma}_{11} &= (\lambda + 2G)\mathscr{E}_{11} \\ &= E\left(\frac{1-v}{(1+v)(1-2v)}\right)\mathscr{E}_{11}. \end{aligned} \tag{25}$$

If we neglect the Poisson effect, since the transverse energies are at least an order of magnitude smaller than the axial energies, $v = 0$, the strain energy is given by

$$PE_{strain} = \int_0^L \int_{A_0} \frac{E}{2} \mathscr{E}_{11}^2 \, \mathrm{d}A_0 \, \mathrm{d}X. \tag{26}$$

The strain energy can be reduced to

$$\begin{aligned} PE_{strain} &= \frac{E}{2} \int_0^L \int_{A_0} \left(u' - Yv'' - Zw'' + \frac{1}{2}v'^2 + \frac{1}{2}w'^2\right)^2 \mathrm{d}A_0 \, \mathrm{d}X \\ &= \frac{E}{2} \int_0^L \left\{ A_0 \left(u' + \frac{1}{2}v'^2 + \frac{1}{2}w'^2\right)^2 + I_z v''^2 + I_y w''^2 \right\} \mathrm{d}X, \end{aligned} \tag{27}$$

where I_z is the area moment of inertia about the z-axis, and I_y is the moment of inertia about the y-axis through the centroid. Note that the expressions are significantly reduced due to the symmetrical cross-section.

The potential energy stored in the base support spring is given by

$$PE_{spring} = \tfrac{1}{2} k (v'^2 + w'^2)|_{0,t}. \tag{28}$$

This assumes that the structure can only bend, not twist.

The kinetic energy of the beam is simply

$$\begin{aligned} KE &= \frac{1}{2} \int_0^L \int_{A_0} \rho [\dot{u}_1^2 + \dot{u}_2^2 + \dot{u}_3^2] \, \mathrm{d}A_0 \, \mathrm{d}X \\ &= \frac{1}{2} \int_0^L \int_{A_0} \rho A_0 [(\dot{u} - Y\dot{v}' - Z\dot{w}')^2 + \dot{v}^2 + \dot{w}^2] \, \mathrm{d}A_0 \, \mathrm{d}X \\ &= \frac{\rho}{2} \int_0^L [A_0 (\dot{u}^2 + \dot{v}^2 + \dot{w}^2) + I_z \dot{v}'^2 + I_y \dot{w}'^2] \, \mathrm{d}X \end{aligned} \tag{29}$$

and the kinetic energy of the point mass is

$$KE_{point\ mass} = \tfrac{1}{2} M_p (\dot{u}^2 + \dot{v}^2 + \dot{w}^2)|_{L,t}. \tag{30}$$

2.2.3. *The governing PDEs and boundary conditions using variational principles*

The Lagrangian is given by

$$\begin{aligned} L &= KE - PE \\ &= \frac{1}{2}\int_0^L \left\{ \rho\left[A_0(\dot{u}^2 + \dot{v}^2 + \dot{w}^2) + I_z\dot{v}'^2 + I_y\dot{w}'^2\right] \right. \\ &\quad \left. - E\left[A_0\left(u' + \frac{1}{2}v'^2 + \frac{1}{2}w'^2\right)^2 + I_z v''^2 + I_y w''^2\right]\right\} \mathrm{d}X \\ &\quad + \frac{1}{2}M_p(\dot{u}^2 + \dot{v}^2 + \dot{w}^2)|_{L,t} - \frac{1}{2}k(v'^2 + w'^2|_{0,t}. \end{aligned} \tag{31}$$

Let $p(X, t)$, $f_y(X, t)$ and $f_z(X, t)$ be distributed loads in the x, y and z directions respectively. The virtual work done by these distributed loads is given by

$$\delta W = \int_0^L [p\delta u + f_y\delta v + f_z\delta w]\,\mathrm{d}X. \tag{32}$$

The variation of the Lagrangian in equation (31) integrated over time is given by

$$\begin{aligned} \delta\int_{t_0}^{t_f} L\,\mathrm{d}t = \int_{t_0}^{t_f}\int_0^L \left\{ \left[-\rho A_0\ddot{u} + EA_0\left(u' + \frac{1}{2}v'^2 + \frac{1}{2}w'^2\right)'\right]\delta u \right. \\ - \left[\rho A_0\ddot{v} - (\rho I_z\ddot{v}')' - \left(EA_0\left(u' + \frac{1}{2}v'^2 + \frac{1}{2}w'^2\right)v'\right)' + (EI_z v'')''\right]\delta v \\ - \left[\rho A_0\ddot{w} - (\rho I_y\ddot{w}')' - \left(EA_0\left(u' + \frac{1}{2}v'^2 + \frac{1}{2}w'^2\right)w'\right)' \right. \\ \left. + (EI_y w'')''\right]\delta w\Big\}\,\mathrm{d}X\,\mathrm{d}t \\ - \int_{t_0}^{t_f}\left\{EA_0\left(u' + \frac{1}{2}v'^2 + \frac{1}{2}w'^2\right)\delta u\Big|_0^L \right. \\ + \left[\rho I_z\ddot{v}' + EA_0\left(u' + \frac{1}{2}v'^2 + \frac{1}{2}w'^2\right)v'^2 - (EI_z v'')'\right]\delta v\Big|_0^L \\ - M_p(\ddot{u}(L, t)\delta u(L, t) + \ddot{v}(L, t)\delta v(L, t) + \ddot{w}(L, t)\delta w(L, t)) \\ + EI_z v''\delta v'|_0^L + kv'\delta v'(0, t) \\ + \left[\rho I_y\ddot{w}' + EA_0\left(u' + \frac{1}{2}v'^2 + \frac{1}{2}w'^2\right)w' - (EI_y w'')'\right]\delta w\Big|_0^L \\ \left. + EI_y w''\delta w'|_0^L + kw'\delta w'(0, t)\right\}\mathrm{d}t. \end{aligned} \tag{33}$$

Using the extended Hamilton's principle,

$$\delta \int_{t_0}^{t_f} (L + W)\,\mathrm{d}t = 0, \tag{34}$$

the equations of motion are given by

$$\rho A_0 \ddot{u} - (EA_0(u' + \tfrac{1}{2}v'^2 + \tfrac{1}{2}w'^2))' = p,$$

$$\rho A_0 \ddot{v} - (EA_0(u' + \tfrac{1}{2}v'^2 + \tfrac{1}{2}w'^2)v')' - (\rho I_z \ddot{v}')' + (EI_z v'')'' = f_y,$$

$$\rho A_0 \ddot{w} - (EA_0(u' + \tfrac{1}{2}v'^2 + \tfrac{1}{2}w'^2)w')' - (\rho I_y \ddot{w}')' + (EI_y w'')'' = f_z \tag{35}$$

and the boundary conditions are given by

$$u(0,t) = 0, \qquad v(0,t) = 0, \qquad w(0,t) = 0, \tag{36–38}$$

$$(EI_z v'' - kv')|_{0,t} = 0, \qquad (EI_y w'' - kw')|_{0,t} = 0, \tag{39, 40}$$

$$EI_z v''|_{L,t} = 0, \qquad EI_y w''|_{L,t} = 0, \tag{41, 42}$$

$$[EA_0(u' + \tfrac{1}{2}v'^2 + \tfrac{1}{2}w'^2) + M_p \ddot{u}]|_{L,t} = 0, \tag{43}$$

$$[\rho I_z \ddot{v}' + EA_0(u' + \tfrac{1}{2}v'^2 + \tfrac{1}{2}w'^2)v' - (EI_z v'')' + M_p \ddot{v}]|_{L,t} = 0, \tag{44}$$

$$[\rho I_y \ddot{w}' + EA_0(u' + \tfrac{1}{2}v'^2 + \tfrac{1}{2}w'^2)w' - (EI_y w'')' + M_p \ddot{w}]|_{L,t} = 0. \tag{45}$$

The boundary conditions in equations (36)–(38) indicate that displacements are zero at $X = 0$. Equations (39) and (40) are the moment conditions at $X = 0$. The bending moments in the y and z directions are proportional to the deflection of the torsional spring in these directions. Equations (41) and (42) state that there are no bending moments at the free end ($X = L$). Equation (43) expresses the fact that the normal force in the x direction is balanced by the inertia force of the point mass in that direction. Equations (44) and (45) indicate that the transverse shear forces are balanced by the inertial forces of the point mass in the respective transverse directions.

Note that $u(X,t)$, $v(X,t)$, and $w(X,t)$ are non-linearly coupled, and therefore, the equations need to be solved simultaneously using numerical methods.

2.3. LINEARIZATION OF EQUATIONS OF MOTION

If we further assume that the rotation squared be small when compared to the linear strain,

$$(\partial v/\partial X)^2 \ll \partial u/\partial X \ll 1 \quad \text{and} \quad (\partial w/\partial X)^2 \ll \partial u/\partial X \ll 1, \tag{46}$$

the Lagrangian in equation (31) becomes

$$\begin{aligned} L &= KE - PE \\ &= \frac{1}{2}\int_0^L \{\rho[A_0(\dot{u}^2 + \dot{v}^2 + \dot{w}^2) + I_z\dot{v}'^2 + I_y\dot{w}'^2] \\ &\quad - E[A_0u'^2 + I_zv''^2 + I_yw''^2]\}\,\mathrm{d}X \\ &\quad + \frac{1}{2}M_p(\dot{u}^2 + \dot{v}^2 + \dot{w}^2)|_{L,t} - \frac{1}{2}k(v'^2 + w'^2)|_{0,t}. \end{aligned} \tag{47}$$

Then the equations of motion are given by

$$\begin{aligned} \rho A_0\ddot{u} - (EA_0u')' &= p, \\ \rho A_0\ddot{v} - (\rho I_z\ddot{v}')' + (EI_zv'')'' &= f_y, \\ \rho A_0\ddot{w} - (\rho I_y\ddot{w}')' + (EI_yw'')'' &= f_z \end{aligned} \tag{48}$$

with boundary conditions

$$\begin{aligned} u(0,t) = 0, \quad v(0,t) = 0, \quad w(0,t) = 0, \\ (EI_zv'' - kv')|_{0,t} = 0, \quad (EI_yw'' - kw')|_{0,t} = 0, \\ EI_zv''|_{L,t} = 0, \quad EI_yw''|_{L,t} = 0, \\ [EA_0u' + M_p\ddot{u}]|_{L,t} = 0, \\ [\rho I_z\ddot{v}' - (EI_zv'')' + M_p\ddot{v}]|_{L,t} = 0, \\ [\rho I_y\ddot{w}' - (EI_yw'')' + M_p\ddot{w}]|_{L,t} = 0. \end{aligned} \tag{49}$$

The equations of motion are decoupled, and we recover the linear elastic equations of motion for each direction.

3. RESULTS ON THE FREE VIBRATION

The free responses of the non-linear three-dimensional rigid and elastic models are considered. The free response of the rigid beam will then be used to gain confidence in the results obtained by the elastic model. For numerical purposes, the properties of the structure given in Table 1 will be used.

The rigid and elastic models are solved numerically using MATLAB. The Runge–Kutta method of order 4 or 5 is used. Fourteen nodes are used for the elastic model.

We can consider two different types of vibration behavior: when the beam moves back and forth in an arbitrary plane and when the beam rotates in three dimensions as shown in Figure 5.

TABLE 1

Beam properties

Beam properties	
Material	Aluminum
Young's modulus, E	73·0 GPa
Density, ρ	2770 kg/m^3
Point mass, M_p	0·236 kg
Torsional spring constant, k	38·8 N/m
Length, L	1·27 m
Outer radius, r_o	0·0127 m
Inner radius, r_i	0·0101 m

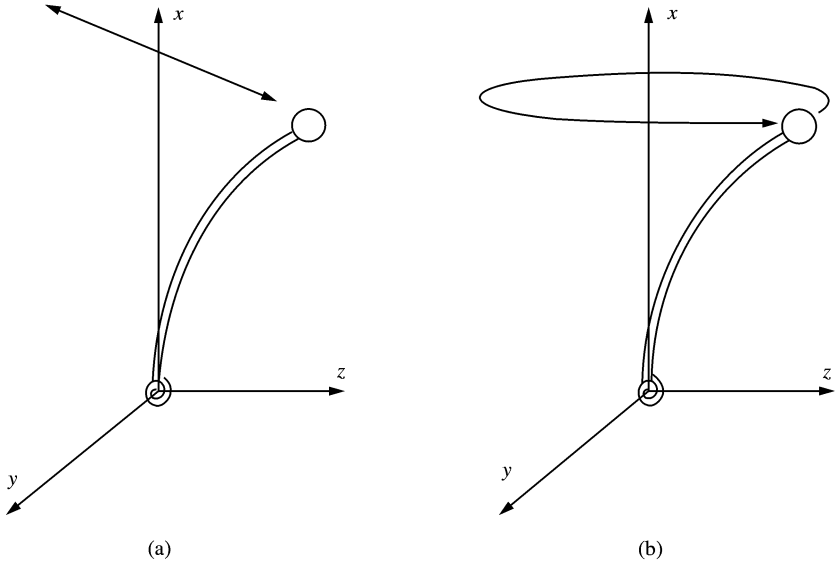

Figure 5. Two types of three-dimensional motion in the absence of external loads: (a) planar 3-D motion; (b) full 3-D motion.

The first type of behavior, Figure 5(a) can be induced by non-zero $\theta(0)$ and zero $\dot{\phi}(0)$ for any $\dot{\theta}(0)$ and $\phi(0)$. When the motion is small enough such that the small angle assumption is valid, the natural frequency of $\theta(t)$ is approximately given by

$$f_{\theta,linear} = \frac{1}{2\pi}\sqrt{\frac{k}{ML^2/3 + M_pL^2 + M(r_o^2 + r_i^2)/4}}. \tag{50}$$

In our case, $f_{\theta,linear} = 1{\cdot}25$ Hz. When the motion is in two dimensions, θ is allowed to turn negative once it passes through $\theta = 0$ as shown in Figure 6(a).

The second type, Figure 5(b), can be induced by non-zero $\theta(0)$ and $\dot{\phi}(0)$ for any $\dot{\theta}(0)$ and $\phi(0)$.

For the rigid case, only a single co-ordinate, θ, is required to describe the motion for the planar model. This co-ordinate can take on positive or negative values as the beam swings

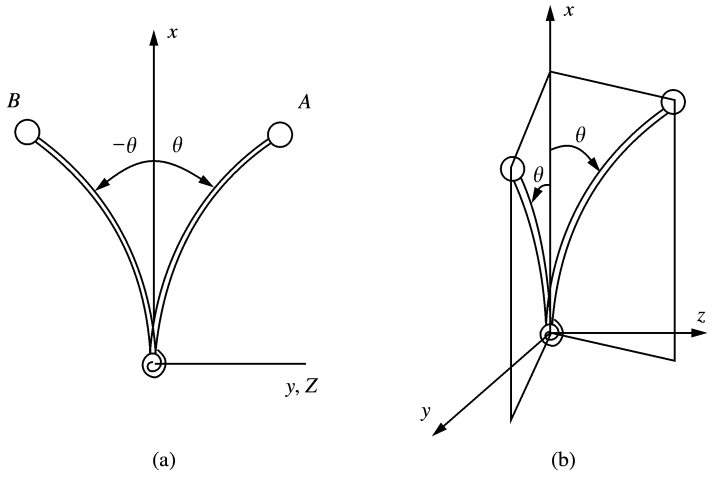

Figure 6. Sign conventions for θ(t): (a) planar model; (b) three-dimensional model.

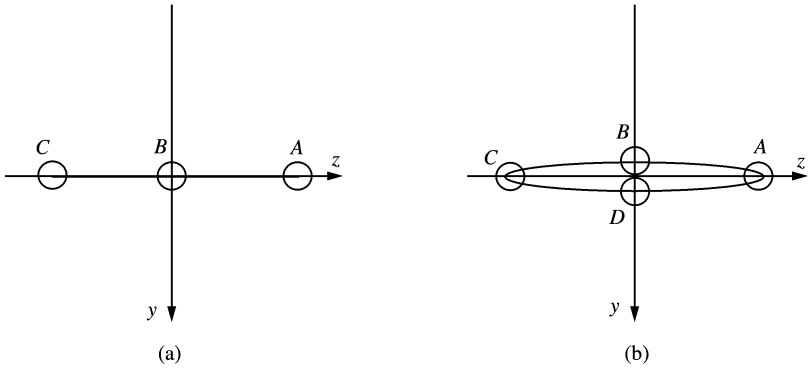

Figure 7. A sample path taken by the tip of the beam: (a) planar model; (b) three-dimensional model.

back and forth through the vertical. On the other hand, for the three-dimensional model, two co-ordinates, θ and ϕ, are required to describe the motion. In this case, θ, which is defined as the angle between the vertical and the beam, is always positive. This can be observed in Figure 6(b).

Continuing this discussion, let us imagine two possible paths taken by the point mass viewed from the top as shown in Figure 7. Figure 7(a) describes a two-dimensional motion and Figure 7(b) a three-dimensional motion generated by slightly disturbing the two-dimensional motion such that points A and C in Figure 7(a) coincide with points A and C in Figure 7(b) respectively. As the point mass in two dimensions goes through ABCBA, the point mass in three dimensions goes through ABCDA. $\theta(t)$ at point C in Figure 7(a) is negative, where $\theta(t)$ at point C in Figure 7(b) is positive but with the same magnitude. Therefore, the fundamental frequency of $\theta(t)$ calculated in three dimensions is equivalent to the fundamental frequency of $|\theta(t)|$ in two dimensions, 2·5 Hz. However, this is a highly idealized case, and we expect that the fundamental frequency of $\theta(t)$ in three dimensions will vary with initial conditions, but be close to 2·5 Hz.

In summary, Figures 5(a), 6(a), and 7(a) depict planar motion, and Figures 5(b), 6(b), and 7(b) depict fully three-dimensional motion.

3.1. THREE-DIMENSIONAL RIGID MODEL

Let us keep in mind the fact that the non-linear rigid model formulation does not make any assumptions regarding the angle of rotation. Therefore, the results are valid for any angle of deflection θ. Here, let us examine the case where the motion is in three dimensions by considering the initial conditions

$$\theta(0) = 0{\cdot}2\,\text{rad}, \quad \dot{\theta}(0) = 0, \qquad \phi(0) = 0, \quad \dot{\phi}(0) = 2\,\text{rad/s}. \tag{51}$$

Figure 8 shows $\theta(t)$ and its power spectral density plot, and Figure 9 shows $\phi(t)$ and its power spectral density plot in logarithmic scale. The decibel here is defined by

$$\text{dB} = 20\log_{10} W(f), \tag{52}$$

where $W(f)$ is the discrete one-sided power spectrum with units of rad^2 (units of θ squared). Since the logarithm of a dimensionless quantity must be taken, the argument of the logarithmic function $W(f)$ is implicitly divided by 1 rad^2 to obtain non-dimensionalization.

The power spectral density plot reveals that the fundamental frequency is about 2·48 Hz for both $\theta(t)$ and $\phi(t)$. It should be noted that the natural frequency of 2·48 Hz for $\theta(t)$ is

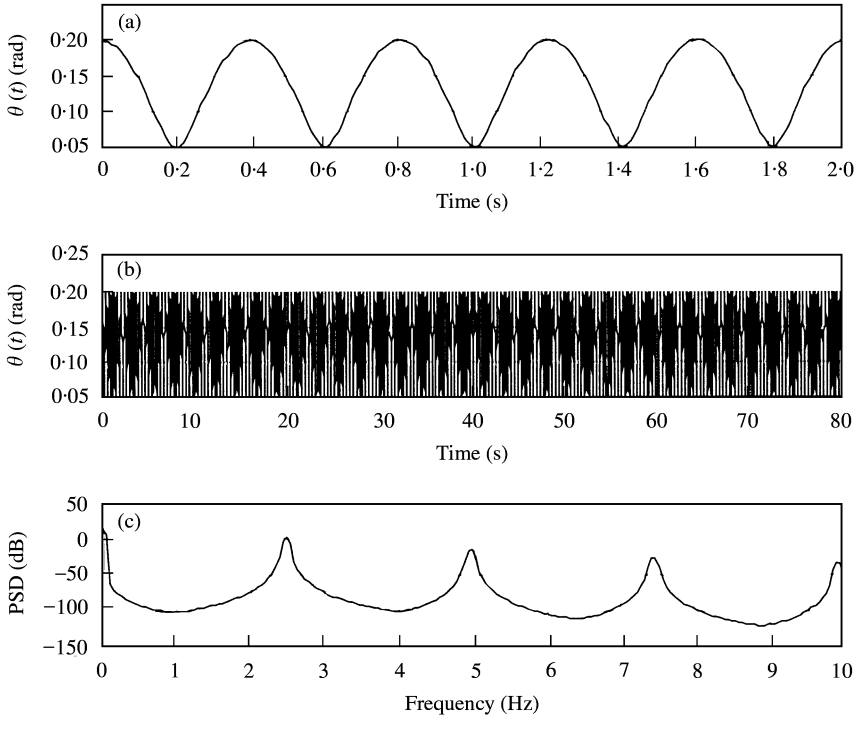

Figure 8. Angle of deflection $\theta(t)$: (a) for early time; (b) over 80 s, and (c) its PSD plot.

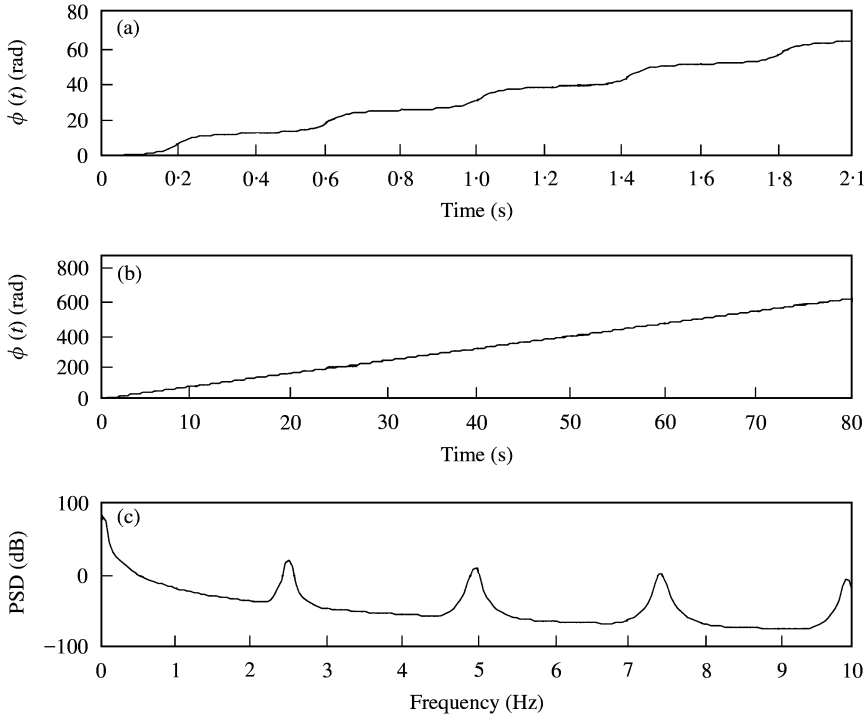

Figure 9. Angle of rotation $\phi(t)$: (a) for early time; (b) over 80 s, and (c) its PSD plot.

consistent with the frequency of 1·25 Hz obtained in equation (50) when the motion is planar and linear.

Figure 10 shows the tip axial displacement, $u(L, t)$. The PSD plot shows that its fundamental frequency is at about 2·5 Hz. This frequency is close to the fundamental frequency of $\theta(t)$ since $\theta(t)$ completes one cycle while $u(L, t)$ also completes one cycle as shown in Figure 7(b). Note that the transverse displacements, $v(L, t)$ and $w(L, t)$, complete half a cycle for each cycle of $\theta(t)$ and $u(L, t)$.

Figures 11 and 12 show the tip transverse displacements, $v(L)$ and $w(L)$, in the y and z directions and their power spectral density plots. The displacements are related to $\theta(t)$ and $\phi(t)$ as shown in Figure 2 and therefore by the following relationships:

$$u(X, t) = X\cos\theta(t) - X, \quad v(X, t) = X\sin\theta(t)\cos\phi(t), \quad w(X, t) = X\sin\theta(t)\sin\phi(t), \qquad (53)$$

where the units are all in meters.

The transverse displacements show a beating phenomenon with two visible frequencies at 1·25 and 0·035 Hz. The envelope or the beat frequency 0·035 Hz is unexpected from the linear analysis. The consequence of this beating phenomenon on the overall response is clearer when the motion is viewed from the top in Figure 13. The horizontal axis in Figure 13 is the transverse displacement in the y direction, and the vertical axis is the transverse displacement in the z direction. The free end follows an elliptical path that rotates in the counterclockwise direction at 0·035 Hz.

In order to understand as to why the path rotates, let us look at what happens for the first 0·81 s as shown in Figure 14. From the figure, we find that θ makes two cycles in about

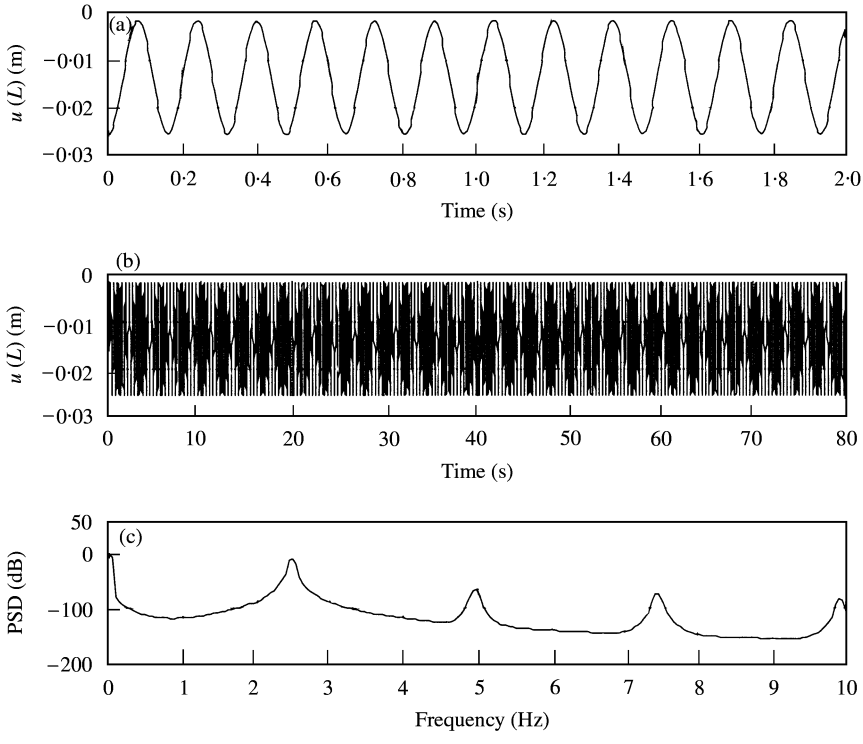

Figure 10. Axial displacement $u(L, t)$: (a) for early time; (b) over 80 s, and (c) its PSD plot predicted by the rigid model.

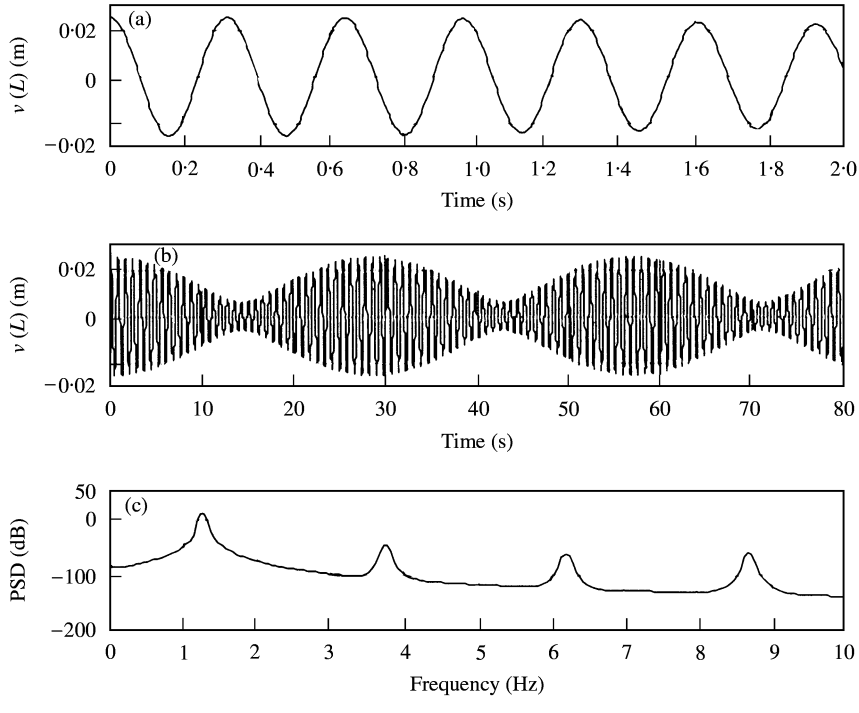

Figure 11. Transverse displacement $v(L, t)$: (a) for early time; (b) over 80 s, and (c) its PSD plot predicted by the rigid model.

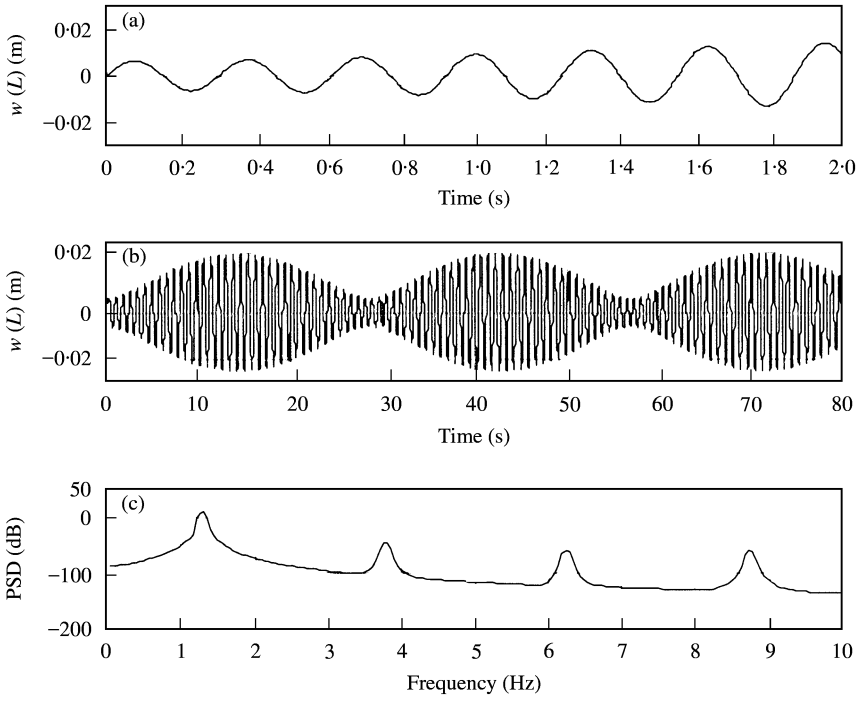

Figure 12. Transverse displacement $w(L, t)$: (a) for early time; (b) over 80 s, and (c) its PSD plot predicted by the rigid model.

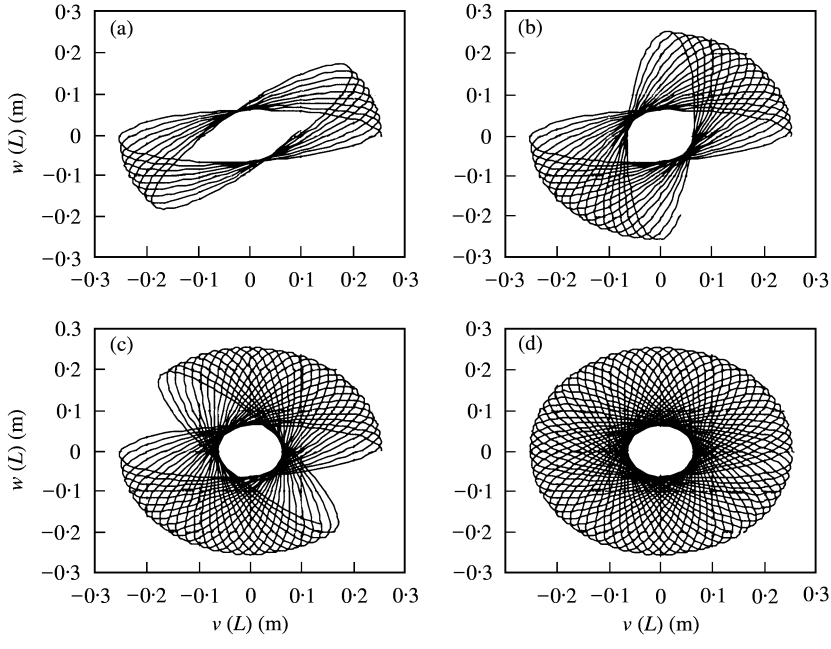

Figure 13. Free response viewed from the top, predicted by the rigid model, for (a) $0 < t < 7{\cdot}1$ s, (b) $0 < t < 14{\cdot}2$ s, (c) $0 < t < 21{\cdot}3$ s, (d) $0 < t < 28{\cdot}4$ s.

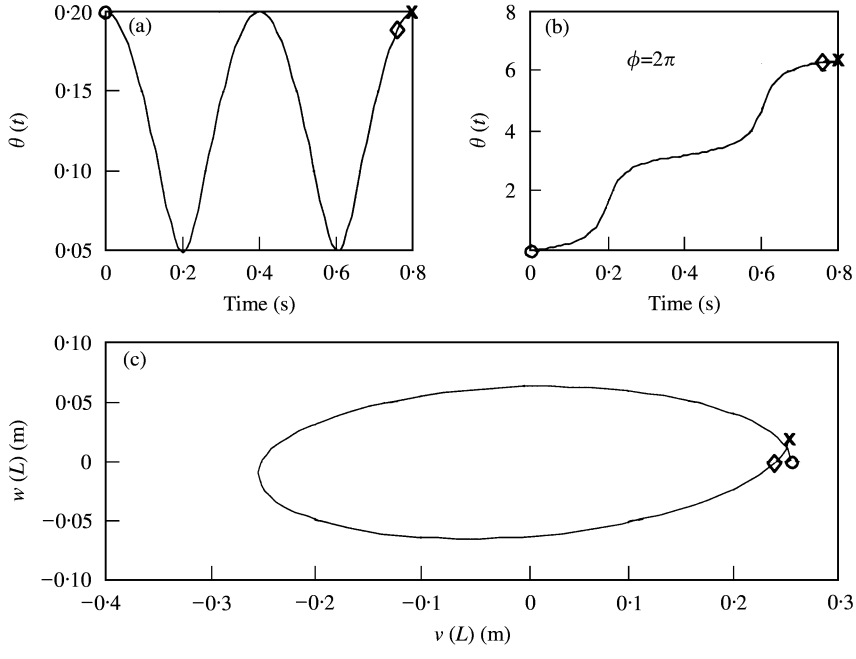

Figure 14. Free response for 0·81 s. The symbol ○ is placed at the initial location, ◇ at $\phi = 2\pi$, and * after θ completes two cycles respectively. (a) $\theta(t)$, (b) $\phi(t)$, (c) $w(L)$.

0·81 s, and ϕ varies from 0 to 2π rad in about 0·76 s. After two cycles of θ have been completed, the free end does not return to its original location so that the path seems to be rotating counterclockwise, and the transverse displacements, $v(X, t)$ and $w(X, t)$, show beating. It is interesting to note that this beating phenomenon does not appear in $\theta(t)$, $\phi(t)$ nor in $u(L, t)$.

Let us further investigate the beating phenomenon that appears in the transverse displacements plot. Let us vary $\theta(0)$ and $\phi(0)$ one at a time. Figure 15 shows $v(L, t)$ with varying time, and Figure 16 shows the top views for $\dot{\phi}(0) = 4$ rad/s and $\theta(0) = 0{\cdot}07$, 0·09, 0·11, and 0·13 rad. They show that as the initial angle increases, the amplitude increases and the beat frequency decreases. Comparing Figure 15(a) with 15(d), where the initial angle almost doubled, the beat frequency decreased almost by a factor of three. While the beat frequency varied with the initial conditions, the "high" frequency inside the envelope remained at about 1·25 Hz.

Figures 17 and 18 show $v(L, t)$ with varying time and the top views for $\theta(0) = 0{\cdot}05$ rad and $\dot{\phi}(0) = 4$, 6, 8, and 10 rad/s. It shows that as $\dot{\phi}(0)$ increases, the beat frequency decreases. Comparing Figure 17(a) and 17(b), where the initial angle is increased by 50%, the frequency decreases by about a factor of two. Again, while the beat frequency varies with initial conditions, the "high" frequency inside the envelope remained at about 1·25 Hz.

In Figures 17(a,b) and 18(a,b), the major axis of the response path coincides with the x-axis at the start of the response. When $\dot{\phi}(0) = 8$ rad/s, the length of the major and minor axes of the elliptical path are very close to each other so that the path is almost circular. Therefore, the path seems stationary. As $\dot{\phi}(0)$ is increased as shown in Figure 17(d), the path continues to rotate in the same direction. In this case, the minor axis coincides with the x-axis in the beginning.

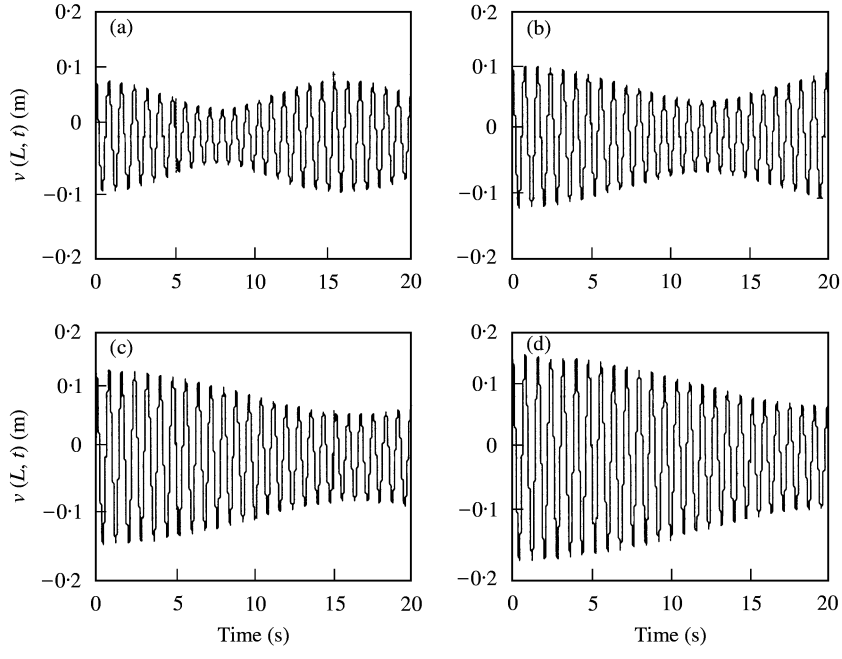

Figure 15. Transverse displacement $v(L,t)$ when $\dot{\phi}(0) = 4$ rad/s. (a) $\theta(0) = 0{\cdot}07$, (b) $\theta(0) = 0{\cdot}09$, (c) $\theta(0) = 0{\cdot}11$, (d) $\theta(0) = 0{\cdot}13$ rad.

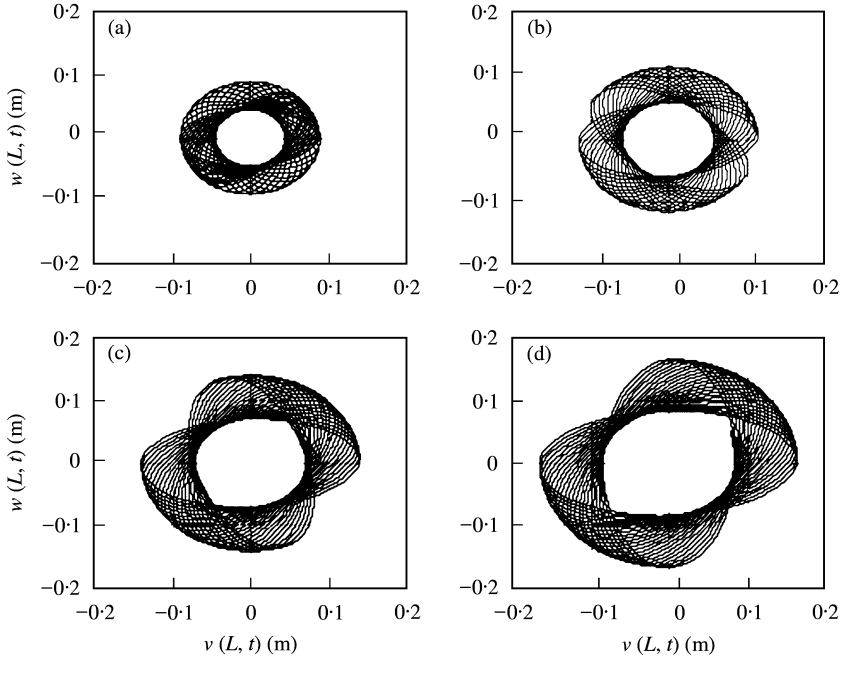

Figure 16. Free response viewed from top when $\dot{\phi}(0) = 4$ rad/s. (a) $\theta(0) = 0{\cdot}07$, (b) $\theta(0) = 0{\cdot}09$, (c) $\theta(0) = 0{\cdot}11$, (d) $\theta(0) = 0{\cdot}13$ rad.

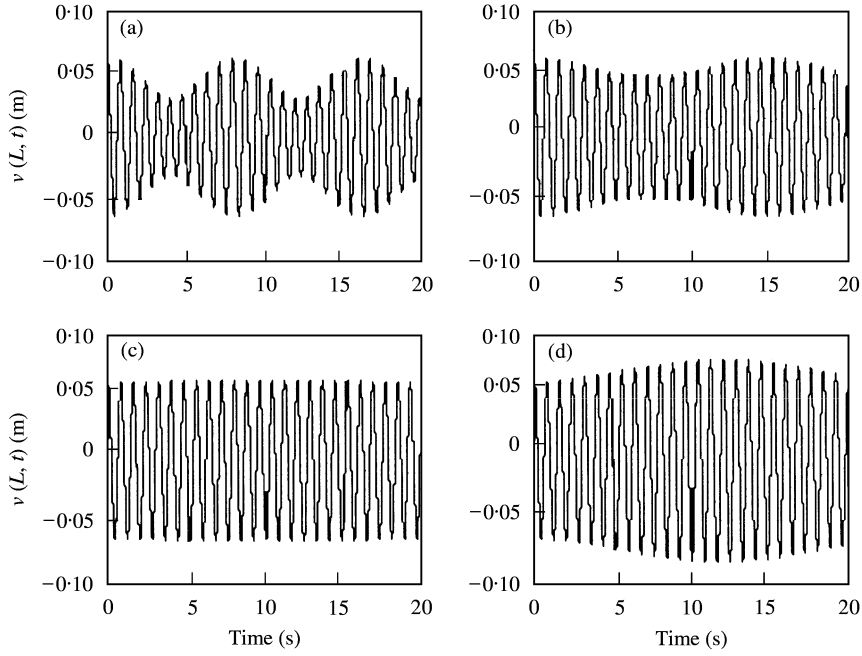

Figure 17. Transverse displacement $v(L,t)$ when $\theta(0) = 0{\cdot}05$ rad. (a) $\dot{\phi}(0) = 4$, (b) $\dot{\phi}(0) = 6$, (c) $\dot{\phi}(0) = 8$, (d) $\dot{\phi}(0) = 10$ rad/s.

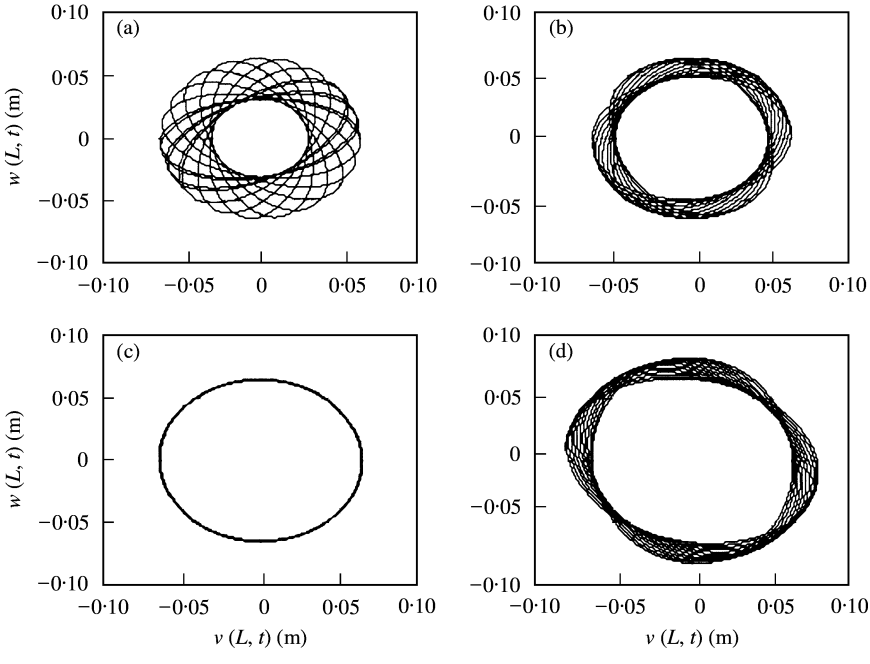

Figure 18. Free response viewed from top when $\theta(0) = 0{\cdot}05$ rad. (a) $\dot{\phi}(0) = 4$, (b) $\dot{\phi}(0) = 6$, (c) $\dot{\phi}(0) = 8$, (d) $\dot{\phi}(0) = 10$ rad/s.

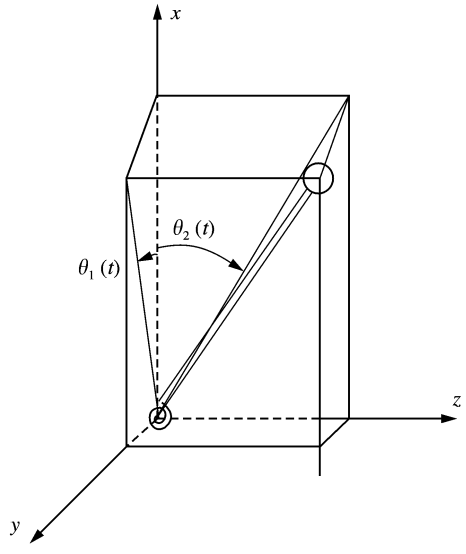

Figure 19. Superposition of two planar models.

From the response plots, we can conclude the following:

1. The fundamental frequencies of $\theta(t)$ and $\phi(t)$ in three dimensions can be approximated by twice the fundamental frequency of $\theta(t)$ in two dimensions.
2. The rotation rate of the elliptical path varies with initial conditions, decreasing with increasing $\theta(0)$ and $\dot{\phi}(0)$.
3. The high-frequency component of the response at 1·25 Hz in the transverse displacements was not affected or affected minimally by the initial conditions.
4. The rotation rate of the elliptical path is more sensitive to $\theta(0)$ than $\dot{\phi}(0)$. Therefore, for a small enough $\theta(0)$, the elliptical path may seem stationary (not rotating). A stationary path indicates that the motions in the xy and the xz plane are *independent* of each other. This is an important result since it implies that if the motion is small (small $\theta(0)$), the motion can be approximated by two planar models. This is also seen in the equations of motion for the elastic model in section 2.3. Three displacements are decoupled when the angle of rotation squared is small compared to the linear strain (equation (46)). For the rigid model, we can make the same analysis such that the transverse displacement of the tip can be obtained by solving the two decoupled equations of motion given by

$$J_2\ddot{\theta}_1 + k\theta_1 = 0, \quad J_2\ddot{\theta}_2 + k\theta_2 = 0, \tag{54}$$

where J_2 is given in equation (12), and $\theta_1(t)$ and $\theta_2(t)$ are the angles of deflection in the xy and xz planes as shown in Figure 19. The transverse displacements are then

$$v(L, t) = L\cos\theta_1(t), \qquad w(L, t) = L\cos\theta_2(t). \tag{55}$$

3.2. THREE-DIMENSIONAL ELASTIC MODEL

Similar response plots are obtained using the non-linear elastic model. The corresponding initial conditions are obtained using equation (53) and are given by

$$u(X, 0) = X(\cos\theta(0) - 1) = -0{\cdot}0199X \text{ m},$$

$$v(X,0) = X\sin\theta(0)\cos\phi(0) = 0{\cdot}199X \text{ m},$$

$$\dot{w}(X,0) = X\dot{\theta}(0)\cos\theta(0)\sin\phi(0) + X\dot{\phi}(0)\sin\theta(0)\cos\phi(0) = 0{\cdot}397X \text{ m/s},$$

$$\dot{u}(X,0) = 0, \quad \dot{v}(X,0) = 0, \quad w(X,0) = 0. \tag{56}$$

The non-linear elastic model is valid for a wider range of angles of deflection from the x-axis ($\partial v/\partial X$ and $\partial w/\partial X$) than the linear elastic model. Recall that the linear elastic model requires that the rotation squared be small when compared to the linear strain,

$$(\partial v/\partial X)^2 \ll \partial u/\partial X \ll 1 \quad \text{and} \quad (\partial w/\partial X)^2 \ll \partial u/\partial X \ll 1, \tag{57}$$

so that the equations of motion are decoupled.

In the non-linear elastic model, the rotation is assumed to be moderate such that

$$(\partial v/\partial X)^2 \sim \partial u/\partial X \ll 1 \quad \text{and} \quad (\partial w/\partial X)^2 \sim \partial u/\partial X \ll 1. \tag{58}$$

The initial conditions in equation (56) are chosen such that the rotation (from the x-axis) squared, $(\partial v/\partial X)^2$, is comparable to the linear strain, $\partial u/\partial X$. Therefore, the linear model is not valid for this set of initial conditions.

Figures 20 and 21 show the tip transverse displacements, $v(L, t)$ and $w(L, t)$, in the y and z directions and their power spectral density plots. The average natural frequency is shown in the PSD plots and is 1·22 Hz, which is lower than that of the rigid beam. This is consistent with our intuition since the rigid beam is "stiffer" than the elastic beam, and the stiffer beam vibrates at a higher frequency. When we look at the transverse displacement plot in

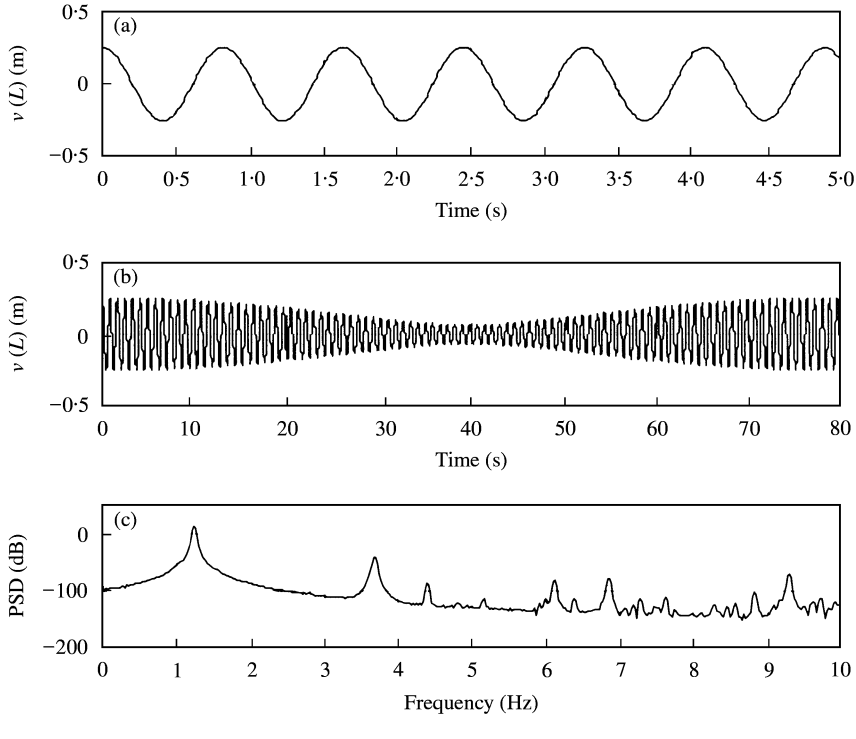

Figure 20. Transverse displacement $v(L, t)$ predicted by the elastic model: (a) $0 < t < 5$ s; (b) $0 < t < 80$ s; (c) PSD.

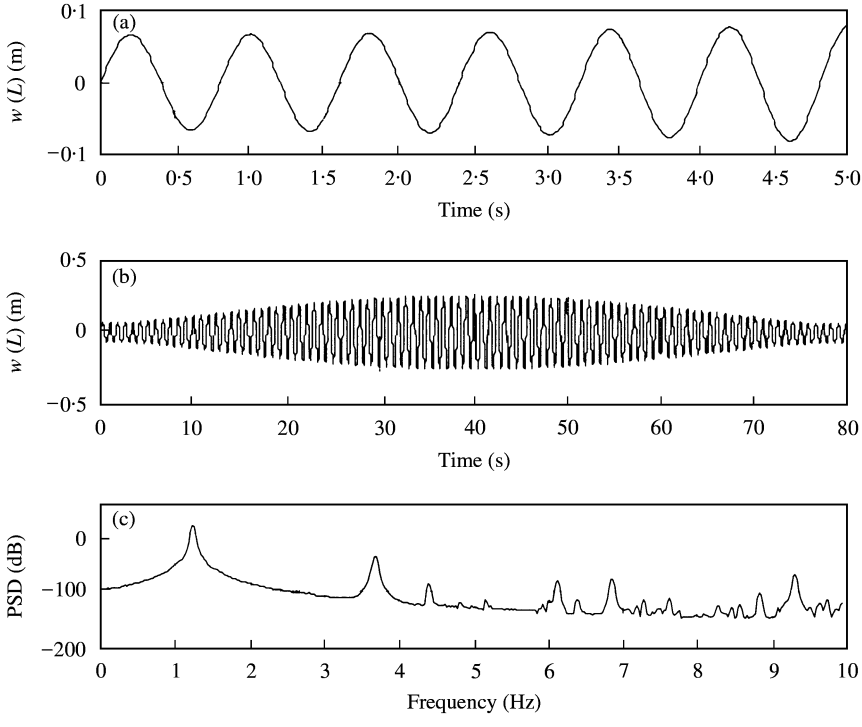

Figure 21. Transverse displacement $w(L, t)$ predicted by the elastic model: (a) $0 < t < 5$ s; (b) $0 < t < 80$ s; (c) PSD.

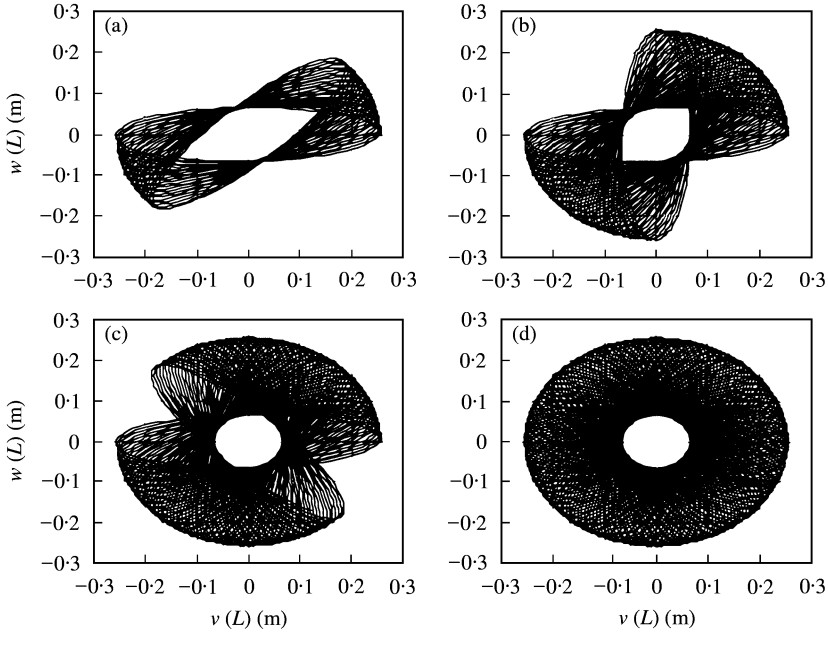

Figure 22. Free response viewed from the top, predicted by the elastic model: (a) $0 < t < 20$ s; (b) $0 < t < 40$ s; (c) $0 < t < 60$ s; (d) $0 < t < 80$ s.

TABLE 2

Results on free vibration

	Fundamental frequency of $u(L,t)$ (Hz)	Fundamental frequencies of $v(L,t)$ and $w(L,t)$ (Hz)	Beat frequency of $v(L,t)$ and $w(L,t)$ (Hz)
Rigid model	2·50	1·25	0·0350
Elastic model	2·44	1·22	0·0126

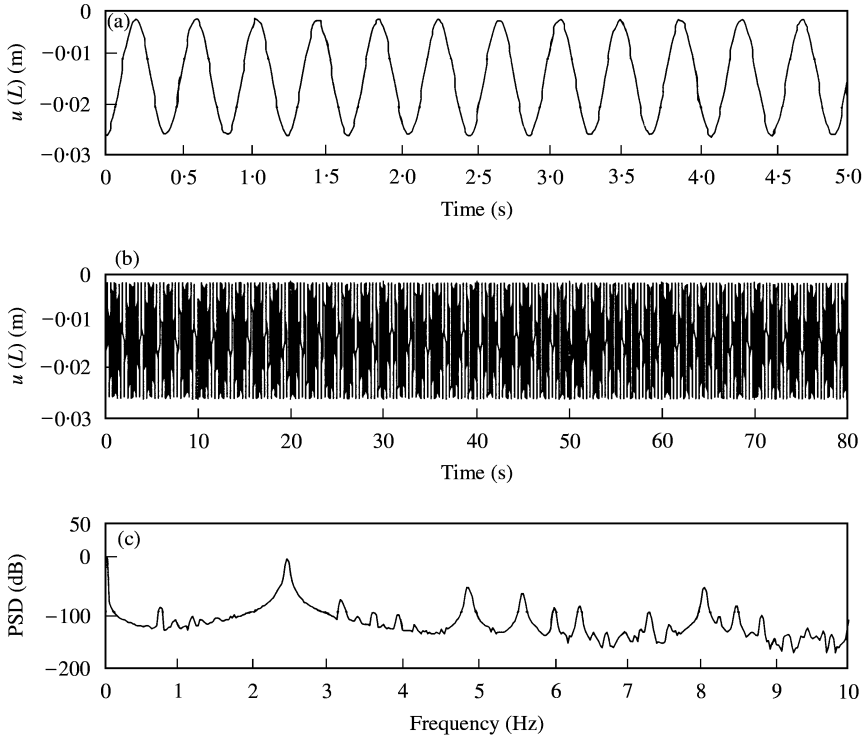

Figure 23. Axial displacement $u(L,t)$: (a) $0 < t < 5$ s; (b) $0 < t < 80$ s; and (c) its PSD plot.

Figures 20(b) and 21(b), the beat frequency seems to be at 0·0126 Hz (period of 79·5 s), which is lower than that of the rigid beam. The top views in Figure 22 show rotating ellipses at 0·0126 Hz. For an easy comparison, the results on the free vibration are summarized in Table 2.

Figure 23 shows the axial displacement $u(L,t)$ and its PSD. The PSD plot shows a dominant frequency at 2·44 Hz, which is twice the fundamental frequency of the transverse motion. This was seen in the rigid case and also in the studies conducted by Han and Benaroya [5, 6].

The numerical results obtained using the three-dimensional elastic model appear reasonable when compared with those of the rigid model.

4. SAMPLE RESULTS FOR THE FORCED RESPONSE OF THE ELASTIC MODEL

In this section, we consider two loading situations. The first case is when a harmonically varying (in time) transverse load is applied in the y direction, and the second is when

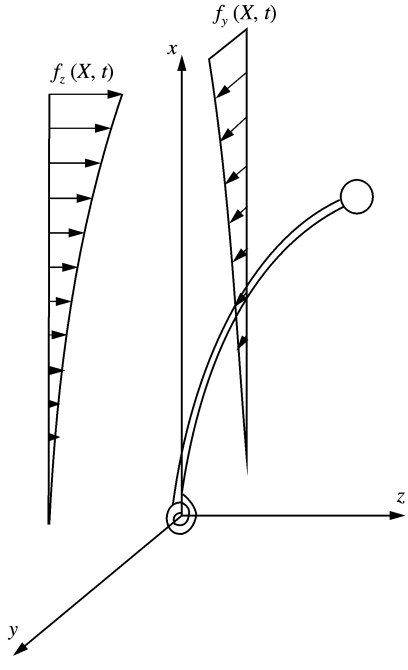

Figure 24. Distributed transverse loads.

TABLE 3

Transverse loads

Case I	$f_y(X, t) = 2(\exp(X) - 1)\cos\omega_f t$	$f_z(X, t) = 0$
Case II	$f_y(X, t) = 2(\exp(X) - 1)\cos\omega_f t$	$f_z(X, t) = 2(\exp(X) - 1)$

a non-harmonic load is applied in the y direction along with a harmonic load in the z direction. In all cases, the transverse loads are exponential in X. The distributed transverse loads in Figure 24 are given in Table 3.

4.1. CASE I: HARMONIC LOADING IN THE y DIRECTION

In this section, we investigate the forced response by varying the forcing frequencies. The initial velocities are set to zero and the initial displacements are given by

$$u(X, 0) = -0{\cdot}002503X \text{ m}, \qquad v(X, 0) = w(X, 0) = 0{\cdot}05X \text{ m}. \tag{59}$$

This is when the beam is initially placed in the first octant. Note that when the initial transverse displacements are given, the initial axial displacement can be found from the equations of motion and boundary conditions.

Figures 25 and 26 show the transverse displacements $v(L, t)$ and their PSD plots when the forcing frequencies are varied from π to 9π at π rad/s increments. The vertical lines in the

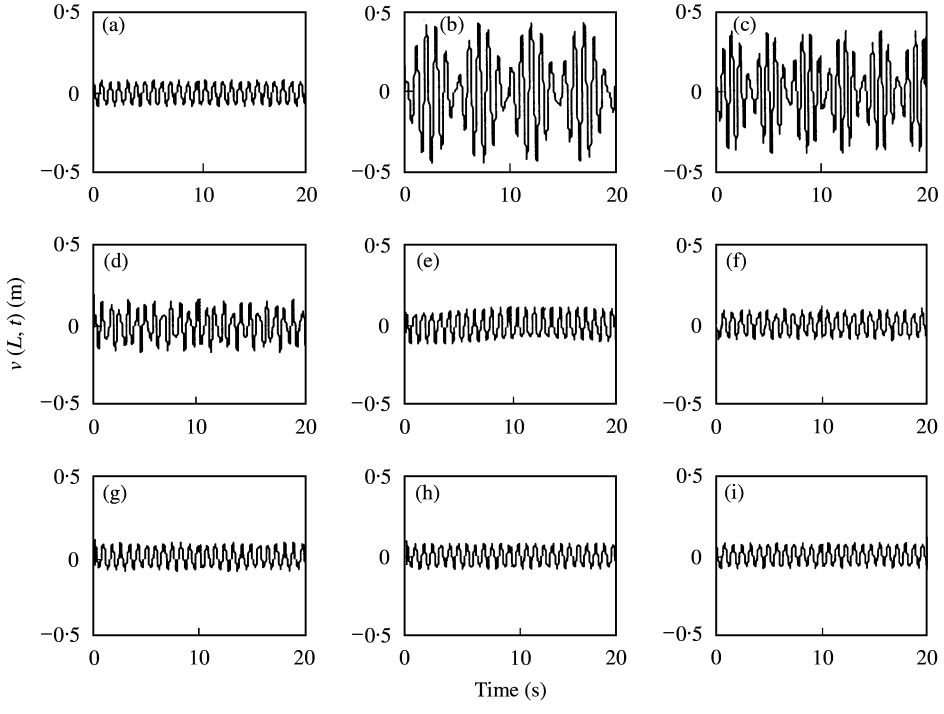

Figure 25. Transverse displacement $v(L,t)$ when $f_y = 2(\exp(X) - 1)\cos\omega_f t$. (a) $\omega_f = \pi$, (b) $\omega_f = 2\pi$, (c) $\omega_f = 3\pi$, (d) $\omega_f = 4\pi$, (e) $\omega_f = 5\pi$, (f) $\omega_f = 6\pi$, (g) $\omega_f = 7\pi$, (h) $\omega_f = 8\pi$, (i) $\omega_f = 9\pi$ rad/s.

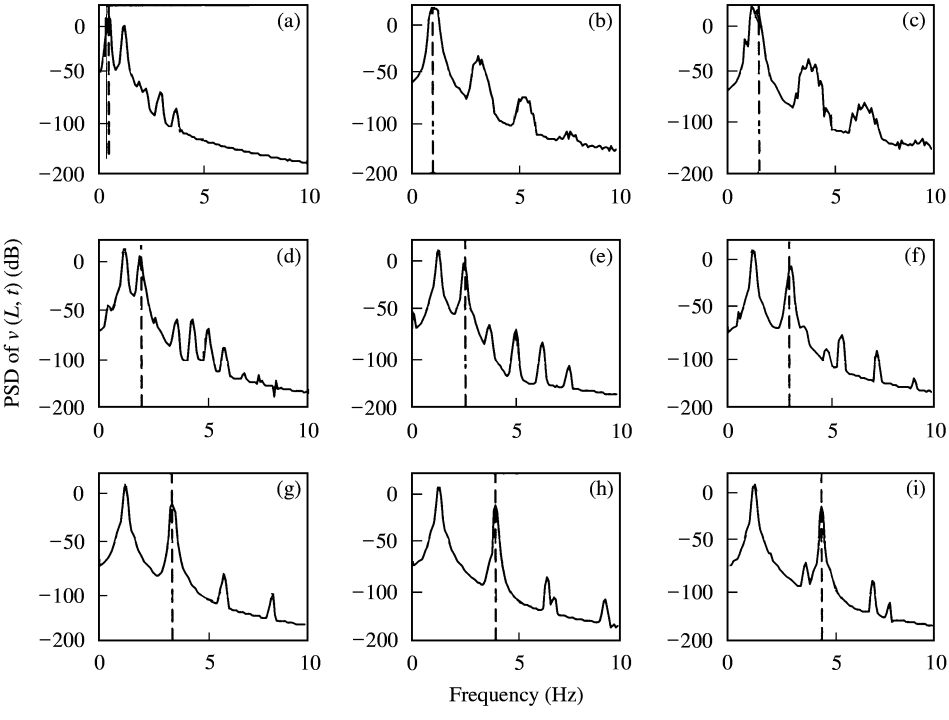

Figure 26. PSD plots for $v(L,t)$ when $f_y = 2(\exp(X) - 1)\cos\omega_f t$. (a) $\omega_f = \pi$, (b) $\omega_f = 2\pi$, (c) $\omega_f = 3\pi$, (d) $\omega_f = 4\pi$, (e) $\omega_f = 5\pi$, (f) $\omega_f = 6\pi$, (g) $\omega_f = 7\pi$, (h) $\omega_f = 8\pi$, (i) $\omega_f = 9\pi$ rad/s.

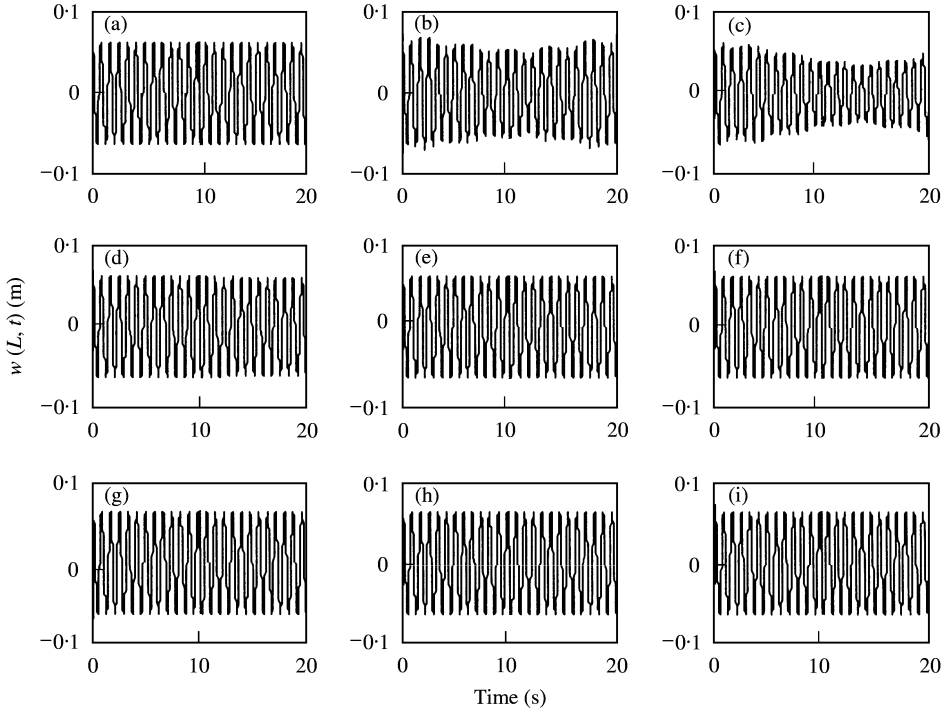

Figure 27. Transverse displacement $w(L,t)$ when $f_y = 2(\exp(X) - 1)\cos\omega_f t$. (a) $\omega_f = \pi$, (b) $\omega_f = 2\pi$, (c) $\omega_f = 3\pi$, (d) $\omega_f = 4\pi$, (e) $\omega_f = 5\pi$, (f) $\omega_f = 6\pi$, (g) $\omega_f = 7\pi$, (h) $\omega_f = 8\pi$, (i) $\omega_f = 9\pi$ rad/s.

PSD plots mark the forcing frequencies. When the forcing frequency is below the fundamental frequency, as shown in Figure 25(a), $v(L,t)$ responds dominantly at the forcing frequency. When the forcing frequency is increased to the vicinity of the fundamental frequency, beating occurs as shown in Figures 25(b,c) and 26(b,c). When this happens, the amplitude of vibration also increases. When the forcing frequency is increased even more, in Figure 26(d)–(f), we see subharmonic resonances of order 1/2, where the system responds at the natural frequency when the forcing frequency is close to twice the natural frequency, and in Figure 26(g)–(i) we see subharmonic resonances of order 1/3. It should be noted that when $v(L,t)$ enters subharmonic resonance, the response looks similar to the free response. That is, $v(L,t)$ vibrates mostly at the fundamental frequency.

Figures 27 and 28 show the transverse displacements $w(L,t)$ and their PSD plots. The transverse displacement in the z direction is minimally affected except for $\omega_f = 2\pi$ and 3π, at which $v(L,t)$ shows beating. However, the amplitude of $w(L,t)$ stays almost constant throughout. In all nine cases, $w(L,t)$ responds at or near the fundamental frequency. The subharmonic resonance discussion above also applies to Figures 28.

Figure 29 shows the view from the top for the first 5 s of motion. Due to the subharmonic response in $v(L,t)$, which resembles the free response and virtually unaffected $w(L,t)$, Figure 29(d)–(i) looks similar to the top views of the free response, the response that we would obtain when the beam is released from the initial position given by equation (59).

Figure 30 shows the phase plots, $v(L,t)$ versus $\dot{v}(L,t)$, and Figure 31 shows the Poincaré maps strobed at the forcing frequency. If the ratio of the forcing frequency to the natural frequency of $v(L,t)$ is a rational number, the Poincaré map will show a discrete number of points. However, in our case, the ratio of the forcing frequency to the natural frequency of

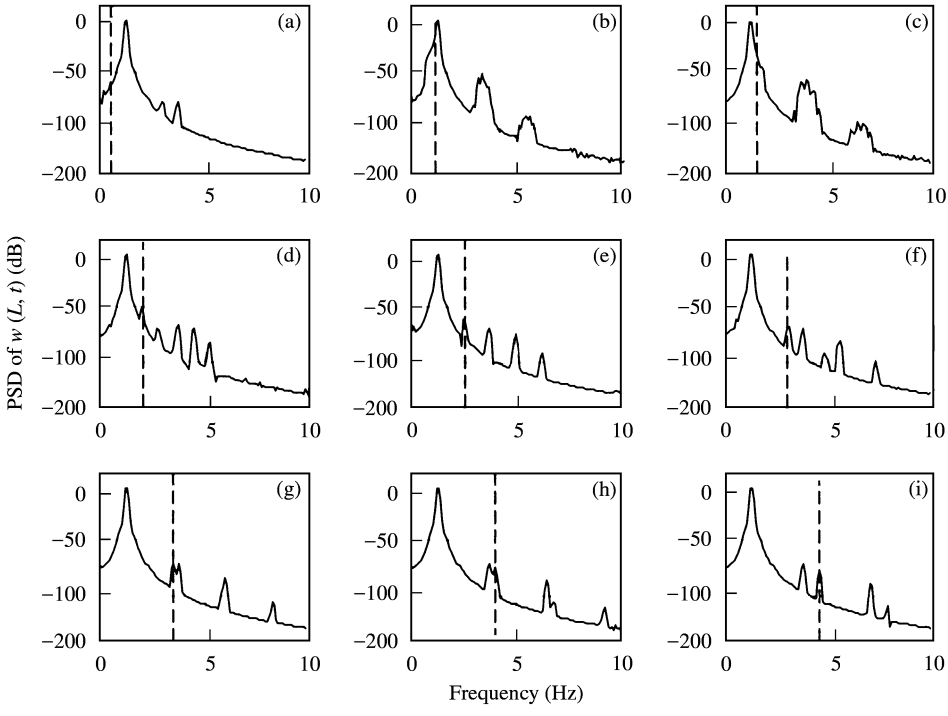

Figure 28. PSD plots for $w(L,t)$ when $f_y = 2(\exp(X) - 1)\cos\omega_f t$. (a) $\omega_f = \pi$, (b) $\omega_f = 2\pi$, (c) $\omega_f = 3\pi$, (d) $\omega_f = 4\pi$, (e) $\omega_f = 5\pi$, (f) $\omega_f = 6\pi$, (g) $\omega_f = 7\pi$, (h) $\omega_f = 8\pi$, (i) $\omega_f = 9\pi$ rad/s.

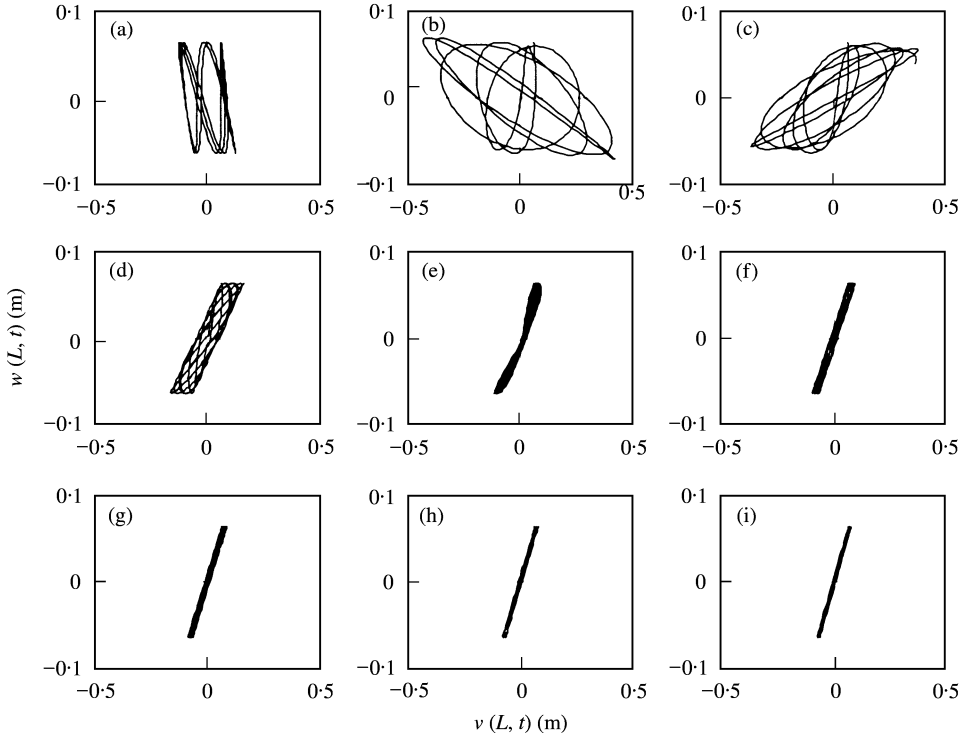

Figure 29. Forced response viewed from the top when $f_y = 2(\exp(X) - 1)\cos\omega_f t$. (a) $\omega_f = \pi$, (b) $\omega_f = 2\pi$, (c) $\omega_f = 3\pi$, (d) $\omega_f = 4\pi$, (e) $\omega_f = 5\pi$, (f) $\omega_f = 6\pi$, (g) $\omega_f = 7\pi$, (h) $\omega_f = 8\pi$, (i) $\omega_f = 9\pi$ rad/s.

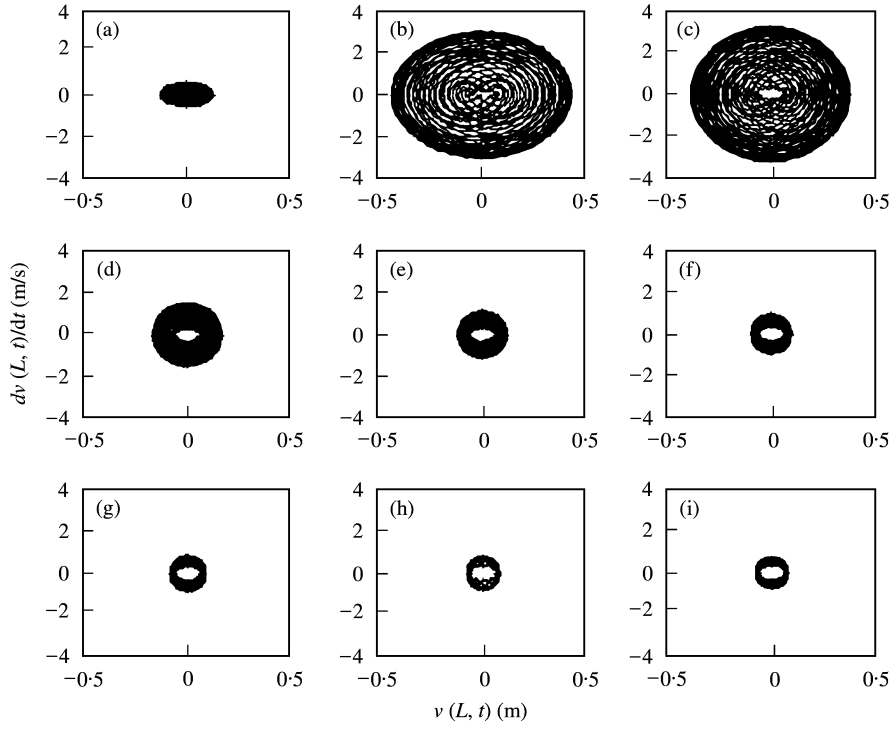

Figure 30. Phase plot for $v(L, t)$. (a) $\omega_f = \pi$, (b) $\omega_f = 2\pi$, (c) $\omega_f = 3\pi$, (d) $\omega_f = 4\pi$, (e) $\omega_f = 5\pi$, (f) $\omega_f = 6\pi$, (g) $\omega_f = 7\pi$, (h) $\omega_f = 8\pi$, (i) $\omega_f = 9\pi$ rad/s.

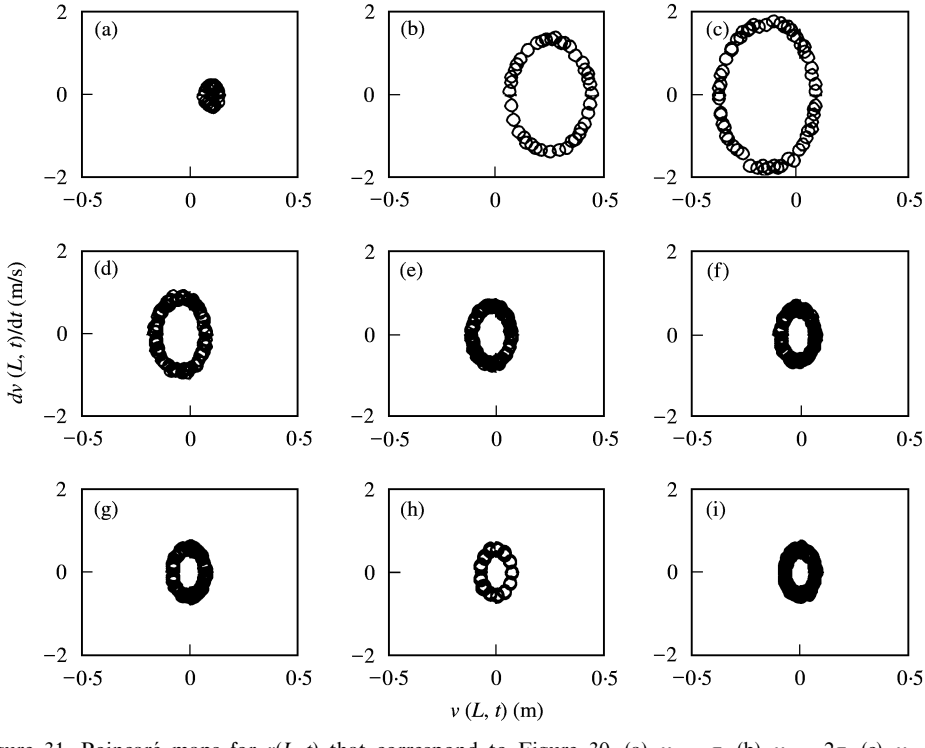

Figure 31. Poincaré maps for $v(L, t)$ that correspond to Figure 30. (a) $\omega_f = \pi$, (b) $\omega_f = 2\pi$, (c) $\omega_f = 3\pi$, (d) $\omega_f = 4\pi$, (e) $\omega_f = 5\pi$, (f) $\omega_f = 6\pi$, (g) $\omega_f = 7\pi$, (h) $\omega_f = 8\pi$, (i) $\omega_f = 9\pi$ rad/s.

$v(L, t)$ may be an irrational number. In that case, $v(L, t)$ does not return exactly to its initial value and the strobe points of the Poincaré map will never repeat. On the Poincaré map, the strobe point will eventually fill in a circle, and the motion is called quasiperiodic [12]. The Poincaré maps in Figure 31 show circular patterns without repeating points, which indicates that our system is quasiperiodic.

4.2. CASE II: HARMONIC AND NON-HARMONIC LOADINGS IN THE PERPENDICULAR DIRECTIONS

Figures 32 and 33 show the response plots when the forcing frequency is π rad/s, and Figures 35 and 36 when the forcing frequency is 6π rad/s. The initial conditions given in equation (59) are used in all cases.

The transverse displacement in the y direction, $v(L, t)$, is almost unchanged from Figure 25(a), where the non-harmonic force in the z direction was not used. In fact, if they were plotted on the same figure, they would overlap. On the other hand, the transverse displacement in the z direction, $w(L, t)$, is shifted to the positive direction from Figure 27(a). However, the frequency of oscillation remains the same. Therefore, for this particular case, we can see that transverse motions in each direction are minimally affected by the forces in the perpendicular directions. That is, the force in the z direction has a minimal effect on the displacement in the y direction, and *vice versa*. The same can be said for the second case when the forcing frequency is 6π rad/s.

5. SUMMARY AND CONCLUSIONS

The equations of motion of a beam supported by a torsional spring at the base and with a point mass at the top were obtained, first by assuming the beam as rigid and second by

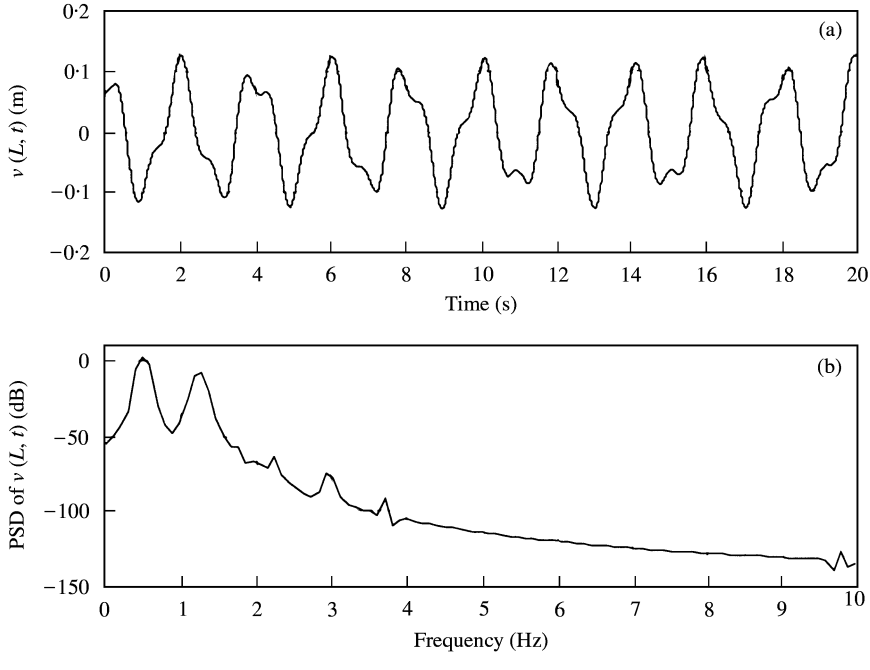

Figure 32. (a) Transverse displacement $v(L, t)$ and (b) PSD plot when $f_y = 2(\exp(X) - 1)\cos \pi t$ and $f_z = 2(\exp(X) - 1)$.

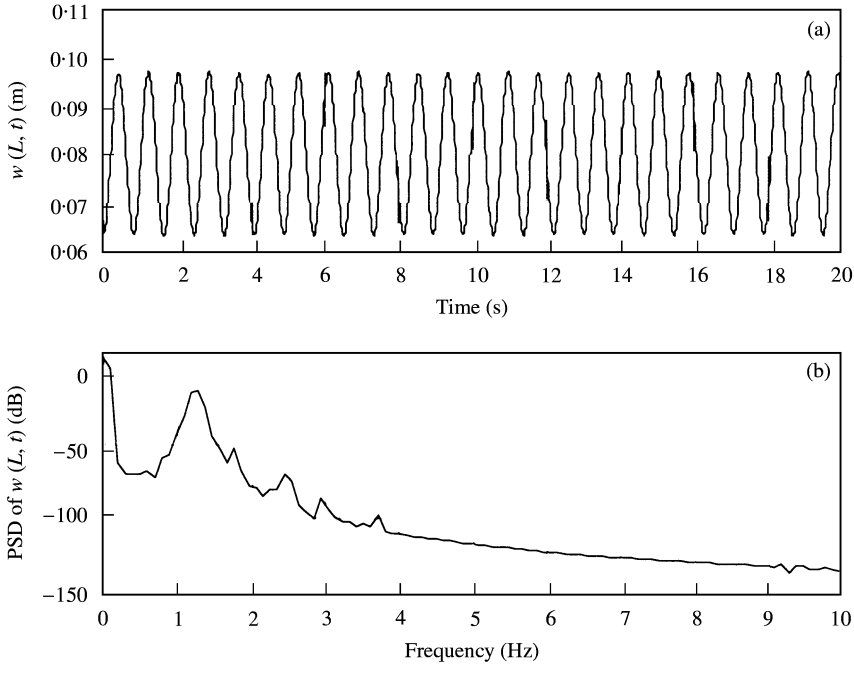

Figure 33. (a) Transverse displacement $w(L, t)$ and (b) PSD plot when $f_y = 2(\exp(X) - 1)\cos \pi t$ and $f_z = 2(\exp(X) - 1)$.

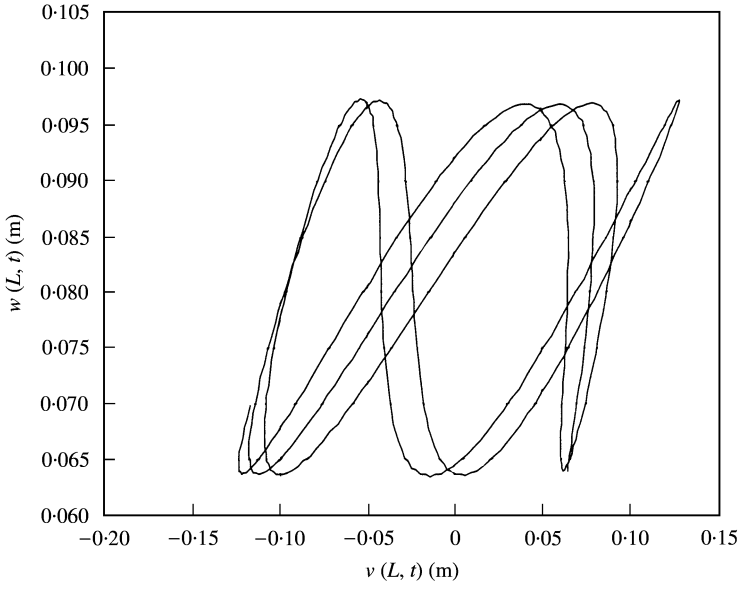

Figure 34. Forced response viewed from the top when $f_y = 2(\exp(X) - 1)\cos \pi t$ and $f_z = 2(\exp(X) - 1)$ for $0 < t < 5$ s.

assuming it as elastic. When the beam was modelled as rigid, the two-degree-of-freedom model, with two angular degrees of the spherical co-ordinate, was employed. When the beam was modelled as elastic, the equations of motion are in terms of displacements in the three directions measured from the original configuration. Kirchhoff's hypothesis and

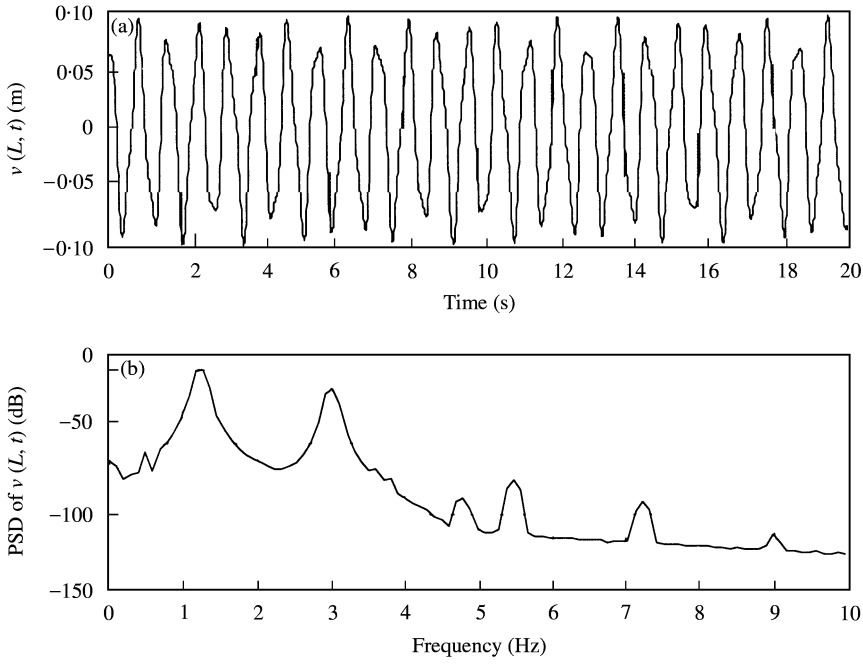

Figure 35. (a) Transverse displacement $v(L, t)$ and (b) PSD plot when $f_y = 2(\exp(X) - 1)\cos 6\pi t$ and $f_z = 2(\exp(X) - 1)$.

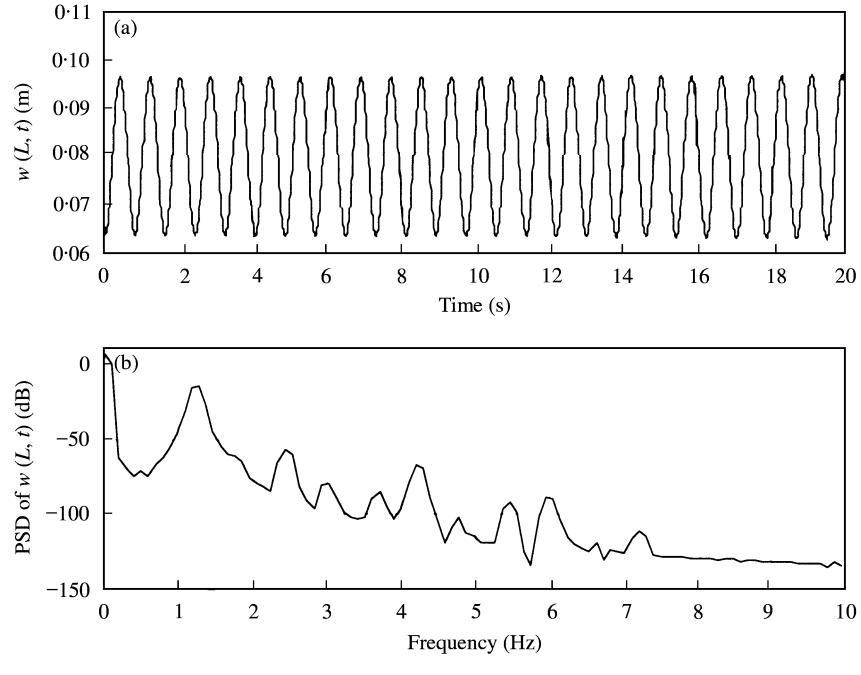

Figure 36. (a) Transverse displacement $w(L, t)$ and (b) PSD plot when $f_y = 2(\exp(X) - 1)\cos 6\pi t$ and $f_z = 2(\exp(X) - 1)$.

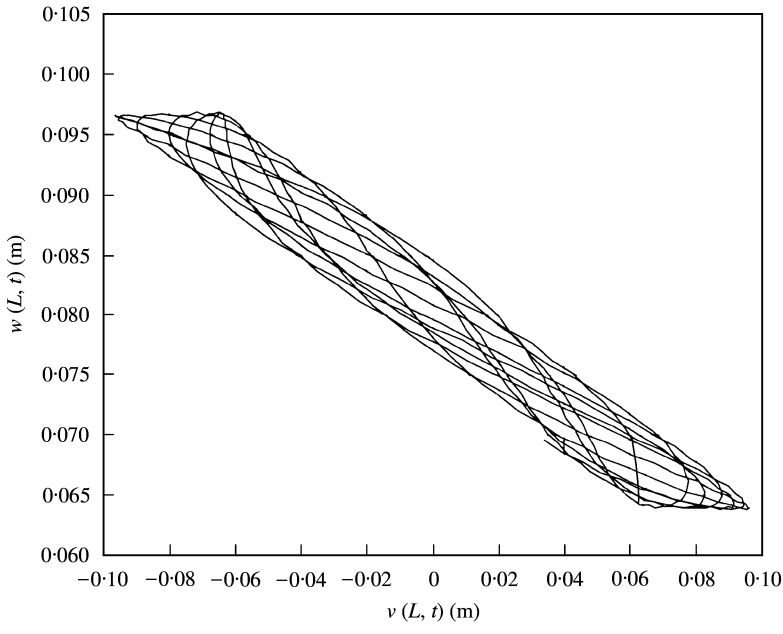

Figure 37. Forced response viewed from the top when $f_y = 2(\exp(X) - 1)\cos 6\pi t$ and $f_z = 2(\exp(X) - 1)$ for $0 < t < 5$ s.

Hamilton's principle were used to obtain the equations of motion and boundary conditions. The equations of motion of the elastic model are coupled non-linear partial differential equations.

The free responses were obtained using both models, and the numerical results compare very well including the fundamental frequency and the non-linear behavior. The rotating path is unique to non-linear three-dimensional models. It was found that the precession rate increases with increasing $\theta(0)$ and $\dot{\phi}(0)$, or, equivalently, increasing $v(X, 0)$, $w(X, 0)$, $\dot{v}(X, 0)$, and $\dot{w}(X, 0)$. Therefore, if those quantities are small enough, the motion in the xy and xz planes can be assumed to be independent, and the response can be analyzed using two planar models.

Once the numerical results of the elastic model were verified, the forced responses due to harmonic and non-harmonic loads were investigated. When the harmonic load was applied in the y direction, the transverse displacement in the y direction goes through a series of responses including beating and subharmonic resonances of orders 1/2 and 1/3. On the other hand, the transverse displacement in the perpendicular direction (z direction) was minimally affected. When the non-harmonic force is added in the z direction, the transverse displacement in the z direction shifted and its amplitude changed while the displacement in the perpendicular direction (y direction) remained about the same. The Poincaré maps strobed at the forcing frequency were plotted, and they reveal that the responses were quasiperiodic for the conditions tested.

It will be interesting to observe chaotic behavior of the damped system for both rigid and elastic models, since most physical systems are damped. Once the transient response diminishes, the Poincaré maps strobed at the forcing frequency will be easier to read and will reveal more about the system.

ACKNOWLEDGMENTS

This work has been supported by the Office of Naval Research Grant No. N00014-97-1-0017. We would like to thank our project manager Dr Thomas Swean for his on-going interest, technical discussions and financial support.

REFERENCES

1. S. CHAKRABARTI 1987 *Hydrodynamics of Offshore Structures*. Southampton, Great Britain: Computational Mechanics Publications, Inc.
2. R. K. JAIN and C. L. KIRK 1981 *Journal of Energy Resources Technology* **103**, 41–47. Dynamic response of a double articulated offshore loading structure to noncollinear waves and current.
3. P. BAR-AVI and H. BENAROYA 1997 *Nonlinear Dynamics of Compliant Offshore Structures*. Lisse, The Netherlands: Swets and Zeitlinger Publishers.
4. R. ADREZIN and H. BENAROYA 1999 *Journal of Sound and Vibration* **220**, 27–65. Non-linear stochastic dynamics of tension leg platforms.
5. R. ADREZIN and H. BENAROYA 1999 *Probabilistic Engineering Mechanics* **14**, 3–17. Response of a tension leg platform to stochastic wave forces.
6. S. HAN and H. BENAROYA 2000 *Journal of Sound and Vibration* **237**, 837–873. Nonlinear coupled transverse and axial vibration of a compliant structure. Part 1: formulation and free vibration.
7. S. HAN and H. BENAROYA 2000 *Journal of Sound and Vibration* **237**, 875–900. Nonlinear coupled transverse and axial vibration of a compliant structure. Part 2: forced vibration.
8. J. F. MCNAMARA and M. LANE 1984 *Journal of Engineering Resources Technology* **120**, 444–450. Particle modeling for articulated risers and loading columns.
9. G. SEBASTIANI, R. BRANDI, F. D. LENA and A. NISTA 1984 *The 16th Annual Offshore Technology Conference*, 379–388. Highly compliant column for tanker mooring and oil production in 1000 m water depth.
10. J. W. LEONARD and R. A. YOUNG 1985 *Engineering Structures* **7**, 74–84. Coupled response of compliant offshore platforms.
11. V. V. NOVOZHILOV 1953 *Foundations of the Nonlinear Theory of Elasticity*. New York: Dover Publications, Inc.
12. G. L. BAKER and J. P. GOLLUB 1996 *Chaotic Dynamics, an Introduction*. Cambridge, U.K.: Cambridge University Press.